

The Effect of Reconstruction Algorithms (Iterative versus Filtered Backprojection) on the Diagnosis of Single Pulmonary Nodules using Thallium-201 and Technetium-99m MIBI SPECT

Rudo Ambayi



Thesis presented in partial fulfilment of the requirements for the degree of

Master of Science in Medical Science (Nuclear Medicine)

at the University of Stellenbosch

**Supervisors: Ms S Ghoorun
Prof P Dupont**

April 2004

“Declaration

I, the undersigned, hereby declare that the work contained in this thesis is my own original work and that I have not previously in its entirety or in part submitted it at any university for a degree.

Signature:

Date:

SUMMARY

This study involved 33 patients, 19 men and 14 women. The age range was wide (20-90 years) and median age was 57 years. These patients had a single pulmonary nodule (SPN) defined radiologically as a well defined, round or oval intrapulmonary lung lesion not associated with atelectasis or adenopathy on chest radiography or computed tomography.

Patients were investigated with Tc-99m MIBI and Tl-201 (25 patients) and with Tc-99m MIBI alone (8 patients). Single photon emission computed tomography images were reconstructed using both iterative reconstruction (Ordered Subsets – Expectation Maximisation: OSEM) and filtered backprojection (FBP), on the Hermes system.

Transverse, coronal and sagittal slices were displayed on the screen using a grey scale. The OSEM and FBP images for each study were co-registered semi-automatically using the multimodality programme on the Hermes. The best slice for the lesion was chosen according to the best view used to locate the SPN on chest radiograph. Regions of interest (ROI) were drawn manually outside the outer margin of the detected lesion, first on the OSEM image. This was automatically mirrored on the co-registered FBP image.

For most patients, the background was automatically mirrored horizontally on the contralateral side, again, first on the OSEM then automatically on the FBP image. Automatic vertical mirroring or manual horizontal mirroring was used when background was found to be in a visually ‘hot’ area like the heart or vertebrae. The average counts and standard deviation of the ROI and background were generated automatically.

Semi-quantitative image analysis was done by calculating the signal-to-noise ratio (SNR) and tumour-to-background (T/B) ratio using the following formulae:

$$\text{SNR} = \frac{\text{Mean counts ROI(lesion)} - \text{Mean counts background}}{\text{Standard deviation background}}$$

$$\text{T/B ratio} = \frac{\text{Mean counts ROI(lesion)}}{\text{Mean counts background}}$$

Detection was found to be the same for the two reconstruction algorithms, that is, every lesion detected by using OSEM could also be detected by using FBP.

However lesion detection did differ between Tl-201 and Tc-99m-MIBI.

Sensitivity and specificity were calculated for different thresholds of SNR and T/B ratios. Receiver operating characteristics (ROC) curves were drawn to represent the different sensitivities and specificities at each threshold. Tuberculosis (TB) was not included in this analysis as uptake of Tl-201 was found to be significantly high and comparable to that of malignant nodules. However the effect of OSEM and FBP on the 'positive' TB nodules was assessed separately. By calculating the area under the ROC curves, Tl-201 using OSEM was shown to be more accurate at differentiating malignant nodules from benign ones than FBP. Although this difference was not statistically significant ($p=0.10$), there was a clear tendency. The two reconstruction algorithms were found to be almost equally accurate, when using Tc-99m-MIBI, the difference between them being considerably insignificant.

In conclusion, it was shown that there is a tendency that OSEM outperforms FBP for studies using Tl-201 but not for Tc-99m-MIBI.

OPSOMMING

Hierdie studie sluit 33 pasiënte in, 19 mans en 14 vroue. Die ouderdomme wissel tussen 20 en 90 jaar met 'n gemiddelde ouderdom van 57 jaar. Elkeen van die pasiënte het 'n enkel longnodule (SPN) op borskas X-straal en/of rekenaar tomografie getoon, wat radiologies gedefinieer word as 'n goed omskewe, ronde of ovaal intrapulmonale longletsel wat nie met atelektase of adenopatie geassosieer is nie.

Pasiënte is met Tc-99m MIBI en Tl-201 (25 pasiënte) of slegs met Tc-99m MIBI (8 pasiënte) ondersoek. Enkelfoton emissie rekenaar tomografiese (EFERT) beelde is met beide iteratiewe rekonstruksie (Ordered Subsets – Expectation Maximisation: OSEM) en gefilterde terugprojeksie (FBP) met die Hermes sisteem gerekonstrueer.

Transvers, koronale en sagittale snitte is in grysskaal op die sisteem vertoon. Die OSEM en FBP beelde vir elke studie is semi-outomaties gekoregister met behulp van die multimodaliteitsprogram op die Hermes. Die optimale snit vir elke letsel is gekies volgens die beste aansig op die borskas X-straal om die SPN te lokaliseer. Gebiede van belang (ROI) is met die hand buite-om die buitenste rand van die letsel getrek op die OSEM beeld en daarna outomaties in die ooreenstemmende area op die gekoregisterde FBP beeld geplaas.

Vir die meeste pasiënte is die agtergrond outomaties as horisontale spieëlbeeld op die kontralaterale kant geplaas, eers op die OSEM en dan outomaties op die FBP beeld. 'n Outomatiese vertikale spieëlbeeld of manuele horisontale verskuiwing van die agtergrondsarea is gedoen indien die agtergrond oorvleuel het met 'n 'warm' area soos die hart of werwels. Die gemiddelde tellings en standaardafwyking van die ROI en agtergrond is outomaties gegenereer.

Semi-kwantitatiewe beeldanalise is gedoen deur berekening van die sein-tot-agtergrond verhouding (signal-to-noise ratio - SNR) en tumor-tot-agtergrond (T/B) verhouding met behulp van die volgende formules:

$$\text{SNR} = \frac{\text{gemiddelde tellings ROI(letsel)} - \text{gemiddelde tellings agtergrond}}{\text{Standaard afwyking van agtergrond}}$$

$$T/B \text{ ratio} = \frac{\text{gemiddelde tellings ROI(letsel)}}{\text{gemiddelde tellings agtergrond}}$$

Opsporing is soortgelyk bevind vir die twee rekonstruksie algoritmes, dit wil sê elke letsel opgespoor met behulp van OSEM kon ook met FBP opgespoor word. Letselwaarneming het egter verskil tussen Tl-201 en Tc-99m-MIBI.

Sensitiwiteit en spesifisiteit is vir verskillende drempels van SNR en T/B verhoudings bereken. 'Receiver operating characteristics' (ROC) kurwes is getrek om die verskillende sensitiwiteite en spesifisiteite by elke drempel te verteenwoordig. Tuberkulose (TB) is nie in hierdie analise ingesluit nie aangesien opname van Tl-201 beduidend hoog en vergelykbaar met die van maligne nodules was. Die effek van OSEM en FBP op die 'positiewe' TB nodules is egter apart beoordeel. Deur berekening van die area onder die ROC kurwes, is getoon dat OSEM van Tl-201 tomografiese data meer akkuraat as FBP was om maligne van benigne nodules te onderskei. Alhoewel hierdie verskil nie statisties betekenisvol was nie ($p=0.10$), is daar wel 'n duidelike neiging gevind. Die twee rekonstruksie algoritmes was byna ewe akkuraat wanneer Tc-99m-MIBI gebruik is, met duidelik geen betekenisvolle verskil tussen die algoritmes nie.

Gevolgtrekking

In hierdie studie is dit getoon dat daar 'n neiging is dat OSEM beter vaar as FBP vir studies met tallium-201 maar nie vir Tc-99m-MIBI nie.

ACKNOWLEDGEMENTS

The completion of this thesis would not be possible without the help I got from people around me. I would therefore like to extend my appreciation, first and foremost to Professor Annare Ellmann, head of Nuclear Medicine department at Tygerberg Hospital, for the immeasurable support and assistance she has provided throughout the whole process. Secondly, I would like to acknowledge and thank Dr Hymne Bouma and Dr James Warwick for all the guidance they have provided both academically and socially.

I would also like to thank Dr Macé Schuurmans for all the clinical data he provided so willingly on the patients used in this study.

My appreciation is also extended to Shivani Ghoorun for all the knowledge she instilled in me especially on the technical aspects of this thesis. I would also like to thank the whole staff of Nuclear Medicine department at Tygerberg Hospital for all my experiences again both academically and socially.

Lastly, I would like to give very special thanks to Professor Patrick Dupont (University of Leuven) for the immense support he has provided during the whole process of making this thesis.

God bless you all!

Rudo Ambayi

SUMMARY	i
OPSOMMING.....	iii
ACKNOWLEDGEMENTS	v
CHAPTER 1: INTRODUCTION.....	1
1.1 INTRODUCTION.....	1
1.2 SINGLE PULMONARY NODULES.....	1
1.2.1 Definition.....	1
1.2.2 Prevalence.....	1
1.2.3 Differential diagnosis.....	1
1.2.4 Importance	2
1.3 EVALUATION OF SINGLE PULMONARY NODULES	2
1.4 IMAGING.....	3
1.4.1 Nodule detection.....	3
1.4.2 Nodule characterization	3
1.5 AIM OF STUDY.....	7
CHAPTER 2: SPECT IMAGING.....	8
2.1 THE GAMMA CAMERA	8
2.1.1 Introduction.....	8
2.1.2 Constituents of a detector	8
2.1.3 Constituents of the processing units	10
2.2 SPECT IMAGING	11
2.2.1 Introduction.....	11
2.2.2 Advantages of SPECT	11
2.2.3 Disadvantages of SPECT.....	11
2.2.4 Types of SPECT camera.....	12
2.2.5 SPECT acquisition.....	12
2.2.6 Factors affecting acquisition.....	13
2.3 ATTENUATION CORRECTION.....	15

2.4 QUALITY CONTROL	17
2.4.1 Introduction.....	17
2.4.2 Uniformity	17
2.4.3 Centre of rotation correction.....	18
CHAPTER 3: RADIOPHARMACEUTICALS	19
3.1 Tl-201	19
3.1.1 Chemistry.....	19
3.1.2 Physical properties.....	19
3.1.3 Preparation	19
3.1.4 Limitations as an imaging agent	19
3.1.5 Mechanism of uptake.....	20
3.1.6 Factors affecting uptake.....	20
3.1.7 Normal biodistribution.....	21
3.1.8 Optimum time for imaging	22
3.1.9 Clinical uses.....	22
3.1.10 Literature review on lung cancer diagnosis	24
3.2 Tc-99m MIBI	25
3.2.1 Chemical properties of Tc-99m	25
3.2.2 Physical properties.....	25
3.2.3 Preparation of Tc-99m MIBI	25
3.2.4 Advantages of Tc-99m as an imaging agent.....	26
3.2.5 Disadvantages of Tc-99m MIBI	26
3.2.6 Mechanism of uptake.....	26
3.2.7 Factors affecting uptake.....	27
3.2.8 Biodistribution	27
3.2.9 Imaging time	28
3.2.10 Clinical uses.....	28
3.2.11 Literature review.....	28

CHAPTER 4: IMAGE RECONSTRUCTION	30
4.1 FILTERED BACKPROJECTION.....	30
4.1.1 Introduction.....	30
4.1.2 Frequency domain	31
4.1.3 Nyquist frequency.....	31
4.1.4 Windows and filters.....	32
4.1.5 Butterworth filters.....	33
4.1.6 Filtered backprojection	33
4.1.7 Advantages of filtered backprojection.....	33
4.1.8 Disadvantages of FBP.....	34
4.2 ITERATIVE RECONSTRUCTION.....	34
4.2.1 Introduction.....	34
4.2.2 Theoretical background	35
4.2.3 Maximum likelihood	36
CHAPTER 5: METHODS	38
5.1 INCLUSION CRITERIA.....	38
5.2 IMAGE ACQUISITION	38
5.2.1 Tc-99m MIBI.....	38
5.2.2 Tl-201	38
5.3 IMAGE RECONSTRUCTION.....	39
5.4 IMAGE ANALYSIS.....	39
5.5 DATA ANALYSIS.....	41
CHAPTER 6: RESULTS	44
6.1 PATIENTS.....	44
6.2 STUDIES	44
6.3 SNR AND T/B RATIO.....	47
6.4 ROC ANALYSIS.....	60
CHAPTER 7: DISCUSSION	63

7.1 OSEM VERSUS FBP	63
7.2 LESION DETECTION	66
7.3 TUBERCULOSIS	67
7.4 ROC ANALYSIS.....	67
7.5 CONCLUSION	69
7.6 SUGGESTIONS FOR FURTHER RESEARCH.....	70
REFERENCES.....	71

CHAPTER 1: INTRODUCTION

1.1 INTRODUCTION

The solitary pulmonary nodule (SPN) continues to be a source of controversy despite being perhaps one of the commonest radiographic abnormalities detected. Once it is discovered, the possibility of its being malignant becomes an immediate concern because malignant lung cancer is one of the most virulent of all cancers with a low overall 5 year survival rate of approximately 10% to 15%¹.

1.2 SINGLE PULMONARY NODULES

1.2.1 Definition

This is radiologically described as a well-defined, round or oval intrapulmonary lung lesion and is not associated with atelectasis or adenopathy². The cut off size remains controversial with some writers quoting 3 cm² and some 4 cm¹ as the cut off point.

In this study, lesions of less than 6 cm were included.

1.2.2 Prevalence

One of every 500 chest radiographs demonstrates a lung nodule. Of these, 90% are incidental findings found unexpectedly in radiographs obtained for unrelated diagnostic workups. This number has increased even further due to incidental findings on chest computed tomography (CT).

1.2.3 Differential diagnosis

Primary bronchogenic carcinoma and benign granulomas constitute the majority of resected pulmonary nodules, accounting together for over 80% of cases. The percentage of each of the above varies between series with an average of 40% respectively in most studies³. Less common diagnoses include hamartomas (6%), solitary metastasis (5%) and bronchial adenoma (2%)⁴.

1.2.4 Importance

Single pulmonary nodule represents a potentially curable stage of bronchial carcinoma.

Bronchial carcinoma is one of the most prevalent and aggressive malignancies. The American Cancer Society estimated that 172 000 cases of bronchial carcinoma will have been reported in 1998 in the USA, 30% of which will present as solitary lesions in the lung⁵.

It was projected that 164 000 individuals in the USA will have been diagnosed with cancer of the lung in 2002 (90200 men, 79200 women)⁶. More disconcerting was that 154 900 of these individuals would succumb to this disease during the year (89200 men, 65700 women). Approximately 1 million people worldwide die of this disease each year. However survival in bronchial carcinoma is closely related to the stage of the disease at the time of diagnosis and a single pulmonary nodule represents a potentially curable stage⁵. Therefore, a timely and accurate diagnosis of the etiology of SPN is essential to providing the patient with malignancy, a potential cure². Primary lung carcinoma rates of 38% have been reported among patients undergoing thoracoscopic biopsies for nodules of less than 1 cm⁷.

The ultimate goal of imaging is to avoid referring a patient with a benign SPN for unnecessary resection, while failing to characterize a small malignant nodule that may be resectable.

Patients with the best prognosis are those who have stage 1A (T1 N0 M0) disease. They have a 61-75% 5 year survival following surgical resection⁸.

1.3 EVALUATION OF SINGLE PULMONARY NODULES

The solitary nodule often produces a diagnostic and management challenge for the chest physician.

The following six factors aid in the decision making⁹:

- ❖ *Calcification* of the nodule is an indicator of a benign lesion especially if homogenous dense, lamellar concentric or central.

- ❖ *Nodule margins*, smooth margins are taken to mean benign disease, irregular spiculated to indicate malignancy.
- ❖ *Previous chest x-rays*: no change in a lesion for two or more years is an indication of a benign lesion.
- ❖ *Smoking history* may influence the physician to favour more aggressive management.
- ❖ *History of previous malignancy* indicates the need for a more aggressive approach. In 80% of patients with previous history of cancer the lesion is metastatic or a new primary tumour.
- ❖ *Patient's age* is an important consideration because the likelihood of the presence of a malignant tumour varies directly with it.

1.4 IMAGING

1.4.1 Nodule detection

The first step is to determine if the nodule is indeed "solitary". This is best done by CT, which can detect very small nodules with greater sensitivity than plain radiographs. Magnetic resonance imaging (MRI) is less sensitive because its spatial resolution is poorer than CT².

1.4.2 Nodule characterization

Once a nodule has been detected it needs to be characterized to estimate the likelihood of malignancy.

1.4.2.1 Plain radiographs

Detection of calcification is particularly important since different patterns are associated with a high likelihood of benign disease. However certain patterns are considered radiologically "indeterminate" meaning they do not increase or decrease the likelihood of malignancy compared to a noncalcified nodule. For example, eccentric or amorphous calcification can represent calcified granuloma engulfed by a malignancy or a dystrophic calcification¹¹.

The rate of failure to diagnose lung cancer on chest x-rays (CXR) varies from 25-90% with different study designs¹⁰. Those missed had significantly smaller lesions (median diameter of 16 mm).

CXRs may also falsely suggest that calcification is present leading to false confidence that the nodule is benign. In a recent series by Berger et al.¹¹, 7% of nodules believed to be "definitely calcified" by CXR lacked calcium on CT and a third of the non calcified nodules on CXR had calcification on CT. Benignity of an SPN, if established by CXR or CT on the basis of a characteristic calcification has been shown to have a likelihood ratio of 0.07¹².

All patients with previous CXR and SPN that is unchanged for 2 years do not require further diagnostic evaluation. However, the growth rate of a lesion is an unreliable predictor of a benign lesion. The CXR is less sensitive than CT for detecting change in size as a doubling in spherical volume may result in a change in diameter of a few millimetres. Low growth rate over 2 years has been shown to have a likelihood of malignancy of 0.01¹².

Despite these shortcomings, CXRs remain intrinsic to the diagnostic work up because they are inexpensive, readily available, quickly obtained and can be read by both physician and radiologist.

1.4.2.2 Chest CT

According to Bethany et al.², Spiral CT is the imaging modality of choice and should be obtained in all newly diagnosed SPNs. It has the advantage of both detecting and characterizing nodules. It can detect synchronous lesions in the lung and metastatic lesions in the liver or adrenals or mediastinal nodes.

It has 50% sensitivity and 89% specificity for detecting mediastinal involvement and 14% sensitivity and 99% specificity for identifying chest wall invasion¹³.

A number of benign aetiologies of SPN have a characteristic appearance on CT. For example, a nodule containing a fat density can be classified as a haematoma. Arteriovenous fistulas demonstrate the presence of a feeding artery and a draining vein as well as contrast enhancement on CT.

Most benign lesions have smooth regular margins, though 21% of malignant nodules have been shown to have the same features ¹⁴.

Malignant nodules may be ill defined with irregular margins and spiculated borders. In fact, 84-90% of spiculated nodules are malignant ¹⁵. Other features which increase likelihood of malignancy are:

- ❖ Size: the great majority of lesions > 2 cm are malignant.
- ❖ Presence of air bronchograms and pseudocavitation.
- ❖ The greater the wall thickness the higher the risk: 84% of all cavitated lesions with a wall of > 15 mm in thickness were malignant ¹⁶.
- ❖ Nodule enhancement is seen more so with malignancy due to hypervascularity, though granulomatous lesions tend to do the same.

CT therefore can be useful in identifying patients with more likely benign lesions and prevent further investigations from being done.

However despite these advantages CT does have some shortcomings. When doing spiral CT the patient is required to hold their breath for up to 30 seconds. This may not be possible with patients with dyspnoea or very poor respiratory function.

1.4.2.3 Magnetic Resonance Imaging

MRI has a very limited role in the diagnosis of single pulmonary nodules. It can be done in a patient who cannot tolerate intravenous contrast.

Even though it provides better anatomic evaluation, its cost is not worth the lower risk of contrast-induced toxicity and the imaging accuracy of CT is as good for most locations of SPNs.

1.4.2.4 Nuclear Medicine procedures

Studies done have shown that nuclear medicine techniques may provide complimentary information with respect to anatomical images. Clinical data indicate that, when used properly, these procedures, in some cases, may provide enough information for the management of lung cancer. Studies done ¹⁷ with Tl-201 and Ga-67 have shown that these can be used successfully to diagnose SPNs. Tl-201 however suffer from a lack of specificity due to uptake in granulomatous inflammation like tuberculosis and

sarcoidosis. Tc-99m MIBI SPECT has been shown to have high specificity and positive predictive value ⁵, which can be helpful in the evaluation of SPNs.

Positron emission tomography (PET) using 18-fluorine-fluorodeoxyglucose (FDG) has been shown to be an excellent imaging modality. FDG is taken up like glucose and phosphorylated. However it cannot enter the normal glycolytic pathway and is thus trapped in the cells. Cells with increased metabolism, as seen in tumours and areas of inflammation, show increased uptake of FDG. The increased metabolic activity appears to be associated with increased activity of glycolytic enzymes namely hexokinase, 6-phosphofruktokinase, and pyruvate dehydrogenase. Also malignant transformation of some cells is associated with increased membrane glucose transport capability due to increased glucose transport proteins. PET scans have shown high sensitivity and specificity ranging from 81-100% and 73-100% respectively with 94% accuracy in the diagnosis of SPN. It has been shown to be as efficacious as transthoracic needle aspiration but with less risk. FDG-PET can potentially change patient management by detecting unsuspected nodal and metastatic disease.

Data for PET scanning for nodules of less than 1 cm has been limited. Even for nodules smaller than 1.5 cm, sensitivity has been shown to decline ¹⁸. The spatial resolution of PET is currently 7-8 mm so imaging of SPNs less than 1 cm is unreliable with the current generation of PET scanners and should not be performed.² Additionally, FDG-PET scanning is limited in its ability to detect low-grade adenocarcinoma, bronchioloalveolar carcinoma and carcinoid syndrome¹. Lesions that are near the limiting spatial resolution of the PET scanner (6 mm on newer systems) may be falsely negative because of the effects of partial volume. False positives are seen and these are thought to be caused by glycolytic activity within activated macrophages for example in active granulomatous diseases such as tuberculosis, sarcoidosis, fungal infection, lipoid pneumonia and talc granulomata following pleurodesis ¹⁹.

Tl-201 SPECT has been shown to have an advantage compared to FDG-PET in a certain type of lung cancer, bronchioloalveolar carcinoma (BAC) ²⁰.

1.5 AIM OF STUDY

Making a firm diagnosis for all pulmonary nodules short of major surgery, especially for small nodules of less than 1 cm, remains problematic. This is evidenced by the continued high rate of resection of benign nodules¹. The reported ranges for the sensitivity and specificity for all these techniques is wide, making the choice of the appropriate technique or diagnostic algorithm controversial.

Currently invasive procedures are being used to make the definitive diagnosis. Fibre optic bronchoscopy and transthoracic needle aspiration biopsy have been used successfully for this purpose. Bronchoscopy may be unreliable in peripheral lesions³. Transthoracic needle biopsy may result in substantial complications (for example pneumothorax and haemoptysis) in 10-20% of patients²¹.

Though a lot of emphasis is currently being placed on FDG-PET because of its high diagnostic accuracy (greater than 90%²²) it still remains unavailable in developing countries. Its other main disadvantage is its false positivity with tuberculosis, which remains prevalent in Southern Africa. Even though neither Tl-201 nor Tc-99m MIBI has shown similar accuracy, they may remain important in the diagnosis of single pulmonary nodules because of their availability in developing countries.

In this study, the effect of two reconstruction algorithms (filtered back projection and iterative reconstruction) on diagnosis of SPNs is investigated.

CHAPTER 2: SPECT IMAGING

2.1 The Gamma Camera

2.1.1 Introduction

A gamma camera, unlike an X-ray machine, does not emit any ionizing radiation but detects radiation emitted from the patient (after injection of a radiopharmaceutical) or other sources. It consists of two main functional units: the detector and the processing unit. The detector is responsible for the primary detection of gamma photons. The key parameters of a planar gamma camera are sensitivity, spatial resolution and energy resolution.

2.1.2 Constituents of a detector

2.1.2.1 Collimator

The collimator consists of channels through which the gamma photons can pass, separated by lead septa. Only photons travelling within the narrow solid angle of acceptance of the collimator can pass unhindered to the detector. Generally the collimator is an inefficient device with only a small fraction (0.02%)²⁷ of the gamma photons emitted from the patient reaching the detector. Parallel hole collimators are currently used for most nuclear medicine studies.

The design of a parallel hole collimator is a compromise between resolution and sensitivity. The interseptal distance to septal length ratio determines the acceptance angle. Long septa results in a small solid angle, so few photons are accepted (low sensitivity) but originate close to the ideal projection line (good spatial resolution).

The in-between septa stop the non-perpendicular rays from reaching the detector. Therefore thickness is determined by the energy of the gamma rays. Thicker septa reduce septal penetration thereby improving resolution at the expense of sensitivity. Increasing the hole size improves sensitivity at the expense of resolution. Sensitivity as a function of distance remains constant whilst resolution degrades with distance. Therefore a trade off between resolution and sensitivity has to be found for any particular acquisition.

The parallel hole collimator provides a direct projection of the organ activity distribution on to the crystal without any change in size. With the widespread availability of large field of view cameras, diverging collimators are now used in special cases. For example, a pinhole collimator can provide the best resolution and image definition for small organs. However its sensitivity is typically poor. This collimator allows magnification changes with distance. Other examples include the cone beam and fan beam collimators, which are specifically designed for cardiac and brain studies.

2.1.2.2 Scintillation crystal

This converts gamma photons into light by a process called scintillation. In an ideal situation photons penetrating the collimator should be completely stopped inside the crystal and deposit all their energy there. The probability of being stopped in the crystal decreases with energy of the gamma photon and increases with thickness of crystal. The gamma photon is absorbed whereby its interaction causes many scintillations (this is the release of visible light). A single sodium iodide (NaI) is used almost exclusively. This is doped with thallium (Tl) to increase light production at room temperature. Its high atomic weight ($Z=53$) enables it to have good stopping power for the gamma photons used in nuclear medicine. The amount of scintillations produced is proportional to the energy of the gamma photon. The crystal is hygroscopic so it is hermetically sealed in a thin aluminium case with an optical window for the photomultiplier tubes.

If circular, the diameter ranges from 25-50 cm and if rectangular, the dimension is up to 60 cm x 38 cm. The most common thickness is 9.5 mm though it can range from 6 mm to 13 mm.

Sensitivity tends to increase with crystal thickness especially for high-energy gamma photons, contrary to resolution, which decreases, thus a compromise is taken. Newer scintillating crystals are becoming available. For example, lutetium oxyorthosilicate, which has a higher stopping power and faster scintillation, results in higher count rates. However, its light output is 75% of NaI (Tl) crystal and since it is radioactive, corrections have to be made for imaging. Cadmium zinc telluride has the advantage that it can be used at room temperature and can be made small and modular resulting in smaller detectors.

2.1.2.3 Photomultiplier tubes

This detects the light produced by the crystals and converts it into an electrical signal. The PMT consists of multiple dynodes (9-12) and the first one is in optical contact with the crystal. This has the ability to release electrons when hit by light (photocathode) through the photoelectric effect. High positive voltage between the dynodes enables the electrons to be accelerated, hitting the next dynode with higher energy thereby liberating more electrons. Each step amplifies the signal with a factor of 3-6 times, resulting in a million times the number of electrons produced at the photocathode. The amplified signal is finally collected at the anode and measured.

Thermal effects or fluctuation in the voltage supply affects the multiplication process.

2.1.2.4 Position circuits /energy

Several tubes in the vicinity detect the light produced by the crystal, and its distance from the gamma photon interaction determines the amount detected by each. From the relative output of each tube and their position, the location of the interaction on the crystal can be estimated with accuracy much greater than the size of the PMTs. This is done by the position weighted network of resistors or capacitors connected to the PMTs output. These produce X and Y position signals, which are proportional to the X and Y position coordinate of the gamma photon interaction in the crystal. The summation of the energy output from only the PMTs in the vicinity provides an energy or Z signal of the gamma photon. Only PMTs in the close vicinity are allowed to contribute to the Z signal to avoid noise from PMTs at a distance from affecting the accuracy of the signal.

2.1.3 Constituents of the processing units

2.1.3.1 Correction circuits

Photomultiplier tubes vary in their response to light and their efficiency in converting it to electrical signals. This results in systematic errors in the position and energy signals. A correction map of these errors is stored in these circuits and these are applied to all position and energy signals to produce an undistorted image.

2.1.3.2 Pulse height analyser

When gamma photons are scattered, they lose some energy and this loss is directly proportional to the scatter angle. Inclusion of these scattered photons causes loss of resolution so it is imperative to exclude as much of these as possible. This is done by the pulse height analyzer, which only produces an output signal if the energy signal from the detector falls within a specified energy window, which has an upper and lower limit. This is called the energy window.

Multiple windows can be used for radionuclides which emit gamma photons with more than one energy, or can be used to do simultaneous acquisition from two different isotopes administered to the patient.

2.2 SPECT Imaging

2.2.1 Introduction

This is based on the reconstruction of tomographic images from projection images, a concept pioneered by Bracewell and Riddle²³ for astronomic applications in 1967 and extended to medical imaging by Shepp and Logan²⁴. It is a technique for producing cross-sectional images of radiotracer distribution in the body. It is called single photon emission computer tomography to distinguish it from positron emission tomography (PET), which records dual photons in coincidence.

2.2.2 Advantages of SPECT²⁵

- ❖ It removes out of plane information thus improving image quality.
- ❖ It has the ability to separate overlapping structures.
- ❖ Allows viewing from multiple planes.
- ❖ Allows for better quantification: for example in tumour/organ volume determination.

2.2.3 Disadvantages of SPECT²⁶

- ❖ Data acquisition, processing and quality control are more time consuming.
- ❖ More demanding in terms of patient compliance.

- ❖ Study interpretation requires an in depth knowledge of the cross-sectional anatomy.
- ❖ Due to the limited system sensitivity and propagation of statistical uncertainty, rotating gamma camera based SPECT is susceptible to noise.
- ❖ The poor system sensitivity and susceptibility to noise occasionally leads to the use of larger activities resulting in higher absorbed doses.
- ❖ Instrumentation is more expensive compared to that for planar imaging.

2.2.4 Types of SPECT camera

2.2.4.1 Singlehead SPECT systems

This consists of one rotating head. Its advantages are that it is relatively inexpensive compared to the multihead system and its quality control is fairly straightforward.

Its disadvantages include relatively low sensitivity resulting in longer acquisition time. This can cause discomfort for the patient, leading to a higher degree of patient motion. An all purpose collimator with a non circular orbit is frequently used as the best compromise to decrease scanning time.

2.2.4.2 Multihead Camera SPECT systems

These systems consist of two or more heads. Offer more spatial/sensitivity characteristics than are available with a single head camera. An assumption is made that the data from different heads are matched in gain and offset so that it can be combined. The advantages include shorter acquisition times. Their higher sensitivity allows for high-resolution collimators to be used and still have acceptable counts in the allotted time. These advantages increase with head number, however the expense of the camera increases substantially with each head.

2.2.5 SPECT acquisition

Acquisition is performed by rotating or stepping the gamma camera around the patient while acquiring data into the digital matrix of a computer. The detector rotates through 180 or 360 degrees around the patient, acquiring images every 2-6 degrees, the latter

being the maximum that should be used. At each step an image is acquired in a 64 x 64 or 128 x 128 matrix for 20-40 seconds.

Movement of the head can either stop at every step (step and shoot) or be continuous.

The step and shoot mode consists of alternately rotating to the next view (step) and acquiring a projection with the camera stationary (shoot).

At any detector angle, data is acquired into the digital matrix of a computer. Each pixel of the matrix receives counts from a narrow 'ray' through the patient. The profile of counts from several rays is called a projection.

According to the theory of computed tomography (CT) projection views acquired over an arc of 180° are adequate for correct reconstruction. In a perfect system opposite projections are mirror images of each other and only one is needed.

However the gamma camera does not have a perfect system so opposing views are not the same because:

- ❖ Resolution degrades with distance between camera and object.
- ❖ A certain percentage of Compton scatter is adopted as photo peak gamma rays due to the finite energy resolution of gamma camera.
- ❖ A certain fraction of the rays are attenuated in an attenuating medium such as a patient and this varies with depth of medium between patient and camera.

For these reasons, 360-degree arc is required for accurate reconstruction in most SPECT studies with the exception being myocardial imaging where 180 degree is standard and in a single detector system where it is more practical. The practical advantage of the 360 degree rotation is that the geometric means of the opposed projections largely, but not entirely, correct for the effects of distance and attenuation.

2.2.6 Factors affecting acquisition

2.2.6.1 Number of angles

Number of angles sufficient to reconstruct faithfully the area of interest depends on the resolution of the camera. This varies with collimator and count rate. In general the following relationship can be used as a reasonable approximation:²⁷

$$N_p \sim \pi M/2$$

where N_p is number of projection angles and M is matrix size.

It however assumes that a proper matrix size has been used. When the number of projection views is less than minimum (that is less than projection image matrix size) streaks may appear in the reconstructed slices. Although in practice coarser angular sampling (30 projections at 6 degree angular increments over a total of 180 degree rotation) may be used for the heart, a finer angular sampling (120 projections at 3 degrees angular increments over a total of 360 degree rotation) may be more appropriate in general ²⁶.

2.2.6.2 Matrix size

The computer divides the gamma camera field of view (FOV) into squares or pixels (picture elements) and two matrix sizes are usually used in SPECT (64 x 64 and 128 x 128). The size of a pixel should ideally be one third of the expected full width at half maximum (FWHM) of the line spread function (LSF) resolution of the SPECT system.

Since the resolution of most SPECT systems is 18-25 mm at centre of rotation a 64 x 64 matrix is perfectly adequate for most imaging applications. For higher resolution the smaller pixel size of 128x128 matrices can be used.

However, despite improving the resolution a 128 x 128 matrix has some disadvantages:

- ❖ Pixel signal to noise ratio may be much poorer because the counts are divided into four times the pixels of a 64 x 64 matrix.
- ❖ Image acquisition and reconstruction will consume more disk space and computer memory.
- ❖ It takes longer to process and film.

However, technology continues to improve speed of computers and reduce costs of disks and memory such that the latter disadvantages will become less significant.

2.2.6.3 Radius of rotation

In rotating gamma camera SPECT, there is a marked depth dependant variation in resolution as the detector rotates in a circle about the long axis of a "non-circular" patient. For the circular orbit, the gamma camera is far from the patient at the anterior and posterior projections resulting in degraded resolution which degrades the overall quality. To avoid this, non-circular orbits (NCO) are used. The orbit is determined manually with

the aid of the technologists or done automatically. This results in the camera moving as close as possible to the patient, thus improving spatial resolution.

The orbit, if step and shoot, may result in a significant source of dead time, that is, the system is not counting when stepping. If the acquisition is continuous, each projection view is somewhat smeared along each row of pixels and will affect the final resolution. This blurring depends on the number of views acquired and it has been noted that at least 120 views over 360 degrees will make the blur insignificant.

2.3 Attenuation correction

Attenuation is the loss of photons either by photoelectric absorption or by Compton scatter. In theory the amount of counts in an image are directly proportional to the absolute concentration of the radiopharmaceutical in that region of interest. The uncertainties in the contribution of scatter and attenuation make quantification of uptake in SPECT images inaccurate. The attenuation of a monochromatic photobeam is described by:

$$I = I_0 e^{-\mu x}$$

where

- I = attenuated gamma ray intensity
- I_0 = original unattenuated gamma ray intensity
- μ = linear attenuation coefficient
- x = depth of attenuating medium.

The linear attenuation coefficient can be derived from the product of the absorber density and the mass coefficient, which depends on the absorber atomic number and the photon energy. It can be broken up into different parts representing the possible interaction of photons with matter: photoelectric effect, Compton scatter and pair production. Only the first two are of importance in SPECT.

From the above equation, it can be calculated that gamma rays from the deeper parts are attenuated more than those from the shallower parts. Thus transaxial reconstructed images appear "colder" in the centre than at the periphery.

In the brain or abdomen, μ is constant because these areas are dominated by soft tissue. Attenuation correction is more complicated in the chest due to the different densities present (bone, lung, and soft tissue) and a constant μ cannot be used.

Two methods are generally used for attenuation correction:

a) Chang's method

A constant μ is used, so this method is appropriate for the abdomen. An ellipse is fitted to the patient's outline in the transaxial images and the depth of each pixel calculated. An approximate or calculated μ (constant) is applied to all the transaxial slices. Due to the presence of scatter, the linear attenuation will be lower than that normally tabulated for a narrow beam without scatter.

The tabulated μ for Tc-99m in water is 0.15 cm^{-1} though it is found that 0.12 cm^{-1} yields satisfactory transaxial images for most applications.

b) Transmission method

This is used for chest studies, for example cardiac. It uses a variable μ , which is dependent on the spatial location of the pixel in the patient. The value of μ is determined by transmission scanning, either with a moving source or fixed sources of different geometries. A μ map is generated, the inverse of which provides the attenuation correction factors.

The source consists usually of long lived isotopes with dissimilar energies to Tc-99m and Tl-201, so a correction factor has to be applied to convert the calculated μ to that appropriate to the radionuclide used.

Accuracy of transmission scan depends on:

- ❖ Strength of transmission source.
- ❖ Lack of patient movement.

- ❖ Attenuation correction algorithm.

Clinical use of attenuation correction is controversial and its widespread use is difficult technologically ²⁸.

2.4 Quality Control

2.4.1 Introduction

Whereas the planar detector quality control measures help ensure high quality images, SPECT imaging requirements place more stringent and additional performance requirement to the detector system. Corrections that have the most significant effects on the reconstructed image are uniformity and centre of rotation and these are done in addition to those done on the camera for planar imaging. The other tests done are:

- ❖ Pixel size calibration.
- ❖ Linearity measurement.
- ❖ Rotational measurements.
- ❖ Energy resolution.
- ❖ Mechanical alignment.
- ❖ Count rate capabilities.

2.4.2 Uniformity

This is defined as a measure of regional sensitivity variation. To avoid artifacts in a reconstructed image, these variations should be less than a few percent. The common artifact seen is a concentric ring or "bull's eye" caused by regional sensitivity variations. These are less pronounced with non-circular orbits and multihead systems since artifacts are blurred.

Variations in uniformity are caused by ²⁹:

- ❖ Poor alignment of PMTs.
- ❖ Failure of one or more PMTs.
- ❖ Spatial nonlinearities.
- ❖ Defect or deterioration of scintillation crystal.
- ❖ Incorrect setting of position and width of PHA window.

❖ High count rate.

For correction, a sensitivity map must be made by acquiring a uniformity image of 60 million counts (for a 64 x 64 matrix) or 120 million counts (for a 128 x128 matrix) using a solid flood source of cobalt-57 or a liquid source with mixed isotopes. These are done with the collimator on for extrinsic flood images or without collimator for intrinsic images. The integral uniformity is calculated as the maximum variation in count density over the entire field of view. The maximum rate of change of counts (differential uniformity) is also calculated as the highest count change and it shows areas with the most sensitivity variations. The camera manufacturer usually provides a program for calculating and saving these values. The uniformity correction is then applied whenever an acquisition is done. A map with the uniformity values is made and this is applied each time an image is acquired to correct for any variations.

2.4.3 Centre of rotation correction

For reconstruction, the algorithm must know the relation between the physical/mechanical axis of rotation and the centre of the projection images; this is the centre of rotation (COR). This allows for a proper position of projection data during backprojection. The COR assumes that at each position, a perpendicular line through the centre of field of view will pass through it. If the COR is accurate, a single point appears as a single point in the reconstructed image with a resolution appropriate for the imaging conditions.

In practice it is not possible to ensure perfect alignment, small deviations between the centre of field of view and the projection of the centre of rotation are seen. For correction, SPECT acquisition of a point source placed near the centre of rotation is done. The deviations are computed; a correction map is calculated and stored in the memory. The saved corrections will then be automatically applied during routine SPECT acquisitions.

CHAPTER 3: RADIOPHARMACEUTICALS

3.1 Tl-201

3.1.1 Chemistry

Thallium is a metallic element of group IIIA. In aqueous solution it is stable and exists as a monovalent cation (Tl^+). Its ionic radius is close to that of potassium (K^+) and hence it exhibits similar biologic behaviour³⁰.

3.1.2 Physical properties

Tl-201 is a radioactive isotope. It decays by electron capture producing X-rays of energy 68-81 keV (94% abundance) and gamma photons of energy 135 keV (3% abundance) and 167.4 keV (10% abundance). It has a half-life of 73 hours. The X-rays are from the daughter atom mercury-201.

3.1.3 Preparation

Tl-201 is produced in a cyclotron by irradiating the natural Tl-203 with a proton beam according to the reaction $Tl-203(p,3n)Pb-201$. The Pb-201 is allowed to decay to Tl-201 for 32 hours. The ions are separated by ion-exchange column chromatography.

Tl-201 is reconstituted with a physiologic solution of sodium chloride and sterilised. Tl-201 is therefore available as an isotonic, sterile and pyrogen free solution for intravenous administration³⁰.

3.1.4 Limitations as an imaging agent

Tl-201 has a number of undesirable properties³¹:

- ❖ Low photon energy, which leads to low resolution images and significant attenuation by overlying soft tissues.
- ❖ A long half-life of 73 hours, which means that the size of the administered dose is restricted to minimise radiation dose.

- ❖ Tl-201 avid tumours cannot be identified in the proximity of high Tl-201 uptake in normal organs. As a result imaging in the pelvis and abdomen has little value.
- ❖ Restricted availability because it is produced by a cyclotron, which makes it more expensive than generator produced radioisotopes.

3.1.5 Mechanism of uptake

It is a potassium analogue. However, thallium uptake and potassium uptake is not identical. Thallium appears to bind to two sites on the (Na-K) ATPase enzyme system compared to one site for potassium. This may explain the prolonged clearance of thallium from the myocardium when compared with potassium clearance³².

As a potassium analogue, thallium activates the sodium potassium (Na-K) ATPase dependent pump. The cellular uptake of thallium is inhibited by ouabain and sodium fluoride, which block the Na-K pump³³.

In the Ehrlich ascites tumour cells model developed by Sessler et al.³⁴, it was found that furosemide inhibits a cotransport system involving potassium, sodium as well as chloride ions and that there is an additive effect of furosemide and ouabain inhibition on thallium-201 uptake.

The transmembrane electric potential gradient has been shown to result in intracellular accumulation³⁵. Tl-201 is accumulated by viable tissue, to a much lesser degree by connective tissue and not at all by necrotic tissue. It is reported to reside in free form in tumour fluids. Only a small amount localises in the nuclear, mitochondrial, and microsomal fractions of the cell³⁶.

3.1.6 Factors affecting uptake

In a review of Tl-201 applications in clinical oncology, Waxman et al.³⁷ summarised the possible factors influencing Tl-201 uptake by tumour cells:

- ❖ The Na-K⁺ ATPase pump activity.
- ❖ Rate of blood flow.

- ❖ Tumour cell viability.
- ❖ Tumour type.
- ❖ Tumour cell membrane function³⁸ for example increased permeability³¹.
- ❖ Leaky capillaries due to immaturity.
- ❖ Calcium ion channel system.

In addition, tumours have ill formed vessels and the retention of Tl-201 correlates well with the percentage of these vessels, i.e. more uptake of Tl-201 is seen with ill formed vessels. Similarly, tumours with higher Tl-201 uptake have higher staining with Ki-67, which is a marker of the number of cells in mitosis and PCNA, which is a marker of specific S phase, indicating a higher mitotic rate³⁹.

3.1.7 Normal biodistribution

Following intravenous injection, Tl-201 chloride is eliminated from the blood circulation with a half of 2.9 minutes³⁰. It is distributed to all parts of the body according to regional blood flow. The heart receives approximately 4% within 10-20 minutes with a myocardial clearance half-life of 4 hours³⁰.

The majority of the dose goes to the:

- ❖ Liver
- ❖ Spleen
- ❖ Skeletal muscle
- ❖ Brain
- ❖ Kidneys
- ❖ Normal thyroid
- ❖ Lachrymal glands
- ❖ Muscles

It is excreted primarily through the kidneys and this is the critical organ. The whole body biological half-life is around 10 days. The effective equivalent dose of Tl-201 is 0.23 mGy/MBq⁴⁰.

3.1.8 Optimum time for imaging

The optimum time for tumour imaging following intravenous injection of Tl-201 has been studied by Schweil et al. ⁴¹. The highest tumour/background ratio was achieved between 11-20 minutes. Imaging can be done between 20 and 60 minutes following intravenous injection. During this time there were minimal changes in the tumour /background ratios.

Because the blood pool activity decreases with time and tumour to background activity contrast becomes better, Chen et al. ⁴² recommended delayed imaging at 3 hours in lymphoma. The latter produced better results when compared to those at 20 minutes.

Gantz et al. ⁴³ imaged 33 patients with soft tissue or osseous masses at 5 minute and 1-4 hours following intravenous injection of Tl-201. In all patients with malignancy there was an increase in the tumour/background ratio from early to late images except in patients who had a biopsy one day prior to scan or who had superimposed fracture. All benign conditions showed a decrease in the ratio between the early and the late images except for a non-united fracture.

3.1.9 Clinical uses

The primary role of Tl-201 in nuclear medicine is its use for myocardial perfusion and for identification of myocardial viability. Non-cardiac imaging applications include parathyroid and tumour imaging. The role in parathyroid imaging was replaced with Tc-99m sestamibi because of simpler technique and better images⁴⁴. Its role in imaging viable tumours is increasing because of problems encountered by magnetic resonance imaging (MRI) and X-ray computed tomography (CT) especially post treatment.

Comparison between Tl-201 and 18-Fluorodeoxyglucose (¹⁸F-FDG) was done by Macapinlac et al. ⁴⁵ and it showed that both are highly reliable in supratentorial tumours and have limitations in infratentorial lesions. Accordingly, Tl-201 can substitute PET were the latter is not available.

Currently Tl-201 is being used for tumour imaging in order to:

- ❖ Differentiate benign from malignant disease and localise sites of biopsy commonly for thyroid, bones, lung, and brain.

- ❖ To determine the grade of malignancy of the tumour most commonly for brain and soft tissue tumours.
- ❖ To evaluate the response of preoperative chemotherapy or radiotherapy and the most common sites are brain, bones, soft tissue and lung.
- ❖ To differentiate post therapy tissue necrosis or fibrosis from local recurrence and the most common locations are the brain, bones, soft tissue and head and neck tumours.

X-ray, computed tomography (CT) and magnetic resonance imaging (MRI) have limitations in addressing these clinical problems. However, PET is more helpful even though there are limitations for its widespread use³¹.

The comparison of uptake between tumour and adjacent normal or background or contralateral tissue has been recommended to differentiate between benign and malignant lesions by many authors⁴³⁻⁴⁶.

In Tl-201 SPECT studies, tumour-to-background ratios of 1.6 - 2.4 are taken to indicate malignancy and lower ratios to indicate benign conditions. It is reported that the higher the ratio the higher the grade of malignancy for example in brain, bone or soft tissue sarcomas. However this ratio is more important if there has been no previous treatment to the lesion.

Lower uptake is seen in early follow-up after surgical treatment or aggressive chemotherapy. In order to improve the diagnosis in this complex situation, especially in brain and soft tissue tumours, early and delayed imaging is recommended at 30 minutes and 2-3 hours.

Van der Wall et al. reported a sensitivity of 88%, a specificity of 94%, a positive predictive value of 88% and a negative predictive value of 94% in bone malignancy⁴⁷.

Tl-201 with low tumour to background ratios has been seen in certain benign lesions like sarcoidosis and tuberculosis³¹.

Tl-201 is being used widely in the localisation of parathyroid adenomas in patients with hyperparathyroidism.

Thallium has a significant role in differentiating malignant from inflammatory lesions for example tuberculosis from Kaposi's sarcoma in AIDS patients. Lee et al.³¹ reported that pulmonary lesions such as lymphomas are Tl-201 negative and gallium-67 positive whilst

pulmonary Kaposi's sarcoma is Tl-201 positive and gallium-67 negative. The accuracy of this was found to be 88%.

3.1.10 Literature review on lung cancer diagnosis

Tl-201 has been described by Cox et al.⁴⁸ as a positive indicator of lung neoplasm. Norihisa et al.⁴⁹ showed that there were significant differences between delayed ratio (uptake ratio of the lesion to the normal lung on delayed scan at 3 hours) and retention index (degree of retention in the lesion) between lung cancer and benign conditions, respectively $p < 0.01$ and $p < 0.05$. It was noted that there seemed to be a difference in Tl-201 uptake among different histological tumour types, with clearance being faster in squamous cell carcinoma than in adenocarcinoma and small cell carcinoma.

The diagnostic accuracy of lung cancer of Tl-201 is challenged by that of F-18-FDG which has been reported to be as high as $> 90\%$ using F-18-FDG PET. However, Higashi et al.²⁰ has shown that Tl-201 SPECT has an advantage compared to FDG PET in a certain kind of lung cancer, bronchioalveolar cell carcinoma (BAC). Tl-201 identified four additional lung cancers that FDG PET did not reveal: three BACs and a well-differentiated adenocarcinoma. Low FDG uptake in BAC is explained by its slow growth rate. FDG uptake in slow growing tumours may be as low as that of benign tumours and some BACs are likely to show false negative studies with FDG PET. In contrast, Tl-201 uptake is depended on a variety of factors (mentioned before) which are not significantly affected by slow growth so significant uptake is seen in slow growing lung cancer.

Tonami et al.⁵⁰ reported 100% sensitivity (147/147) for pulmonary malignant lesions of > 20 mm in diameter with Tl-201 SPECT. However, 70% of the benign lesions also had significant uptake so the measurement of a retention index was proposed. No significant difference in the delayed ratio was found between malignant and benign lung nodules but a significant difference in the retention index was observed⁵⁰.

Due to the poor resolution and significant attenuation of Tl-201, it is reasonable to assume that PET will have better lesion detectability especially for small sized lesions than Tl-201 SPECT.

Tl-201 avid tumours cannot be identified in the proximity of high uptake. Higashi et al.²⁰ missed moderately differentiated adenocarcinoma near the myocardium with Tl-201 SPECT.

If both FDG and Tl-201 are available then FDG is the first choice for imaging lung tumours, but for suspected BACs Tl-201 SPECT may be recommended²².

In our setting of unavailable PET, Tl-201 remains a useful tool for the diagnosis of single pulmonary nodules.

3.2 Tc-99m MIBI

3.2.1 Chemical properties of Tc-99m

It is a group VIIB element, which has seven electrons beyond the noble gas electronic configuration. It can easily lose the seven electrons to form the +7 Oxidation State. The other members of the group are manganese (Mn) and rhenium (Re) and the three form a triad.

3.2.2 Physical properties

Tc-99m is produced from a molybdenum-99 generator and it decays by isomeric transition producing a monoenergetic gamma ray of 140 keV. It has a half-life of 6 hours. It decays to Tc-99 which has a long half-life of 2.1×10^5 year which makes it almost stable.

3.2.3 Preparation of Tc-99m MIBI³⁰

Pertechnetate ($^{99m}\text{TcO}_4^-$) is added to lyophilised MIBI with stannous chloride. The vial is mixed thoroughly and heated in an upright position in boiling water for 10 minutes. This mixture is stable for 6 hours. Tc-99m MIBI is a member of a chemical family referred to as isonitriles and is chemically hexakis 2-methoxyisobutyl isonitrile. This radiopharmaceutical is a monovalent cation in which Tc-99m is surrounded by six isonitrile ligands.

3.2.4 Advantages of Tc-99m as an imaging agent

- ❖ A mono-energetic gamma ray of 140keV is easily collimated and yields a sufficient number of photons.
- ❖ The half-life of 6 hours is long enough to obtain desired diagnostic information.
- ❖ The half-life is short enough to cause minimal exposure to patient and personnel.
- ❖ Lack of beta emissions lowers radiation dose to patients and personnel.
- ❖ Its daughter molecule is almost stable further limiting the radiation dose to the patient.
- ❖ Because of the low radiation dose it can be given in higher doses enabling dynamic and SPECT studies to be done.
- ❖ It is easily available since a generator produces it and this allows for easy patient scheduling⁵¹.

3.2.5 Disadvantages of Tc-99m MIBI

Its Tc-99m label would suggest some advantages over Tl-201. However it has some similar disadvantages with Tl-201 for lung and breast imaging due to its high uptake by the heart and soft tissues. Its large hepatobiliary clearance poses a problem for intra-abdominal imaging³⁶.

3.2.6 Mechanism of uptake

Tc-99m sestamibi is a positively charged lipophilic complex and therefore its uptake is mostly by passive diffusion. It has been shown that sestamibi is attached to a low molecular weight protein in the cell lysosome and this is found in viable tissue³⁶.

The cationic charge and lipophilicity of Tc-99m MIBI, the mitochondria and plasma membrane potentials of the tumour cell and the cellular mitochondria content may play a significant role in the uptake^{52,53}.

Strongly negative mitochondrial and plasma membrane potentials can promote concentration of the agent within the mitochondria. Therefore, alterations in cell metabolism, which affect this potential, could influence accumulation of sestamibi. It has been shown that malignant tumours maintain higher (more negative) mitochondrial and

plasma membrane potentials secondary to their increased metabolic requirements, which could promote accumulation of sestamibi in these tissues ⁶.

3.2.7 Factors affecting uptake

Uptake is proportional to:

- ❖ Amount of blood flow.
- ❖ Leaky capillaries.
- ❖ Increased membrane permeability.
- ❖ Transmembrane diffusion driven by negative electrical potential gradients ⁵⁴.
- ❖ Cellular mitochondrial content ⁵⁴.

Sestamibi is also a substrate for the P-glycoprotein, which is found in cells that over express the multidrug resistance gene (MDR1). Characteristically, tumour cells pump out a variety of products including sestamibi. Thus washout of sestamibi from tumour in association with the MDR1 gene may have prognostic and therapeutic implications that remain to be characterised ⁵⁵.

3.2.8 Biodistribution

Tc-99m MIBI is cleared fairly rapidly from the blood, with less than 5% remaining in the blood after 10 minutes. The heart takes up about 4%. It accumulates in a range of organs including:

- ❖ Liver
- ❖ Thyroid
- ❖ Salivary glands
- ❖ Kidneys
- ❖ Lung
- ❖ Muscles

Progressive clearance of lung and liver activity with tracer excretion through the kidneys and via the hepatobiliary system is seen.

3.2.9 Imaging time

Hassan et al.⁵¹ studied 19 patients with lung lesions (13 malignant, 6 benign) using Tc-99m MIBI. The dynamic study demonstrated that the uptake of MIBI in malignant tumours is fast, most probably perfusion related and the peak uptake is reached within the first minute. Therefore, a short (30 minutes) kinetic assessment has been suggested. There is minimum washout from the tumour site and heart by 30 minutes. Yoshihiro et al.⁵² found that the positivity rate was 96% for the early images and 89% in the delayed images whilst that for Tl-201 was 98% for both early and delayed images. This showed that delayed imaging does not increase the positivity rate so early imaging is adequate for sestamibi.

3.2.10 Clinical uses

- ❖ Tc-99m MIBI has been successfully evaluated for myocardial imaging and is used to assess myocardial perfusion.
- ❖ Used to diagnose parathyroid adenoma due to its slower clearance from tumour than from thyroid.
- ❖ Widely used in mammoscintigraphy as aid in diagnosis of breast cancer.
- ❖ Its association with the overexpression of the MDR1 gene indicates a possible role in prediction of tumour response to therapy.
- ❖ The use of Tc-99m MIBI before and after brain tumour therapy may be an indicator of efficacy of a specific type of chemotherapy³⁸.

3.2.11 Literature review

Radionuclide imaging of lung cancer with gallium-67 and Tl-201 has been disappointing due to the poor physical properties, long waiting time after injection as well as lack of specificity⁵. Tl-201 studies in tumours suffer from lack of specificity due to the occasional reported Tl-201 uptake in sarcoidosis and granulomatous nodal tuberculosis³¹. Tc-99m MIBI imaging for the diagnostic evaluation of patients with lung cancer has been investigated and its role in this setting is not firmly established because the reported experiences are controversial.

Wang et al.⁵⁶ compared results of Tc-99m MIBI (planar and SPECT imaging) with those of F-18-FDG PET in 19 patients with proven lung cancer. For lung lesions, the diagnostic sensitivity of planar MIBI was 83% while those of MIBI SPECT and FDG PET were both 100%. Quantitative analysis of lung tumour uptake of MIBI and FDG showed that the latter was significantly higher ($p < 0.001$). However MIBI SPECT imaging may still be useful to evaluate patients with lung tumours and may be considered an alternative when PET is not available.

Minai et al.⁵ did a prospective study on patients with single pulmonary nodules. For malignancy the overall specificity was 100%, sensitivity 85.7%, positive predictive value 100%, and negative predictive value 57%. Quantitative uptake of MIBI correlated with the diameter of the nodule. This relationship was statistically significant ($p = 0.02$). This preliminary study showed that Tc-99m MIBI has a very high specificity and positive predictive value for malignant single nodules and might be a useful non-invasive diagnostic modality in their management.

CHAPTER 4: IMAGE RECONSTRUCTION

4.1 FILTERED BACKPROJECTION

4.1.1 Introduction

The counts obtained from each ray are placed (backprojected) in all the image pixels along that ray.

This backprojection is performed for all projections at various angles. Therefore it is a composite of all the ray sums of multi-angled, two-dimensional views²⁷. In this way, an image of radionuclide distribution is constructed in the image memory.

Bruyant et al.⁵⁷ defined the backprojection operator as:

$$a(x, y) = \int_0^{\pi} g(s, \theta) d\theta$$

where $g(s, \theta)$ is defined as the number of counts at any location, $s = x \cos(\theta) + y \sin(\theta)$ along the detector head at angular position θ and the quantity $a(x, y)$ as the estimated number of photons emitted at any point (x, y) of the transverse slice in the field of view. The assumption is that the quantity $a(x, y)$ is proportional to the tracer concentration.

The function g is the projection of a on the crystal. This means that $g(s, \theta)$ is the sum of the counts recorded in any time at point s . Under ideal conditions, projections at angles between π radians (180°) and 2π (360°) do not provide new information because they are symmetrical. Acquiring projections for many distinct angular positions of the detector can solve the inverse problem where we have to determine a when g is measured.

Backprojection represents the accumulation of all the rays that pass through the point (x, y) .

It can be shown mathematically that in the ideal case, we can find the original function a when we apply the backprojection on projections which are first filtered by a ramp filter in the frequency space (see later). This is called filtered backprojection.

4.1.2 Frequency domain

Spatial information can be converted to the frequency domain by the mathematical process known as Fourier transformation (FT). According to this transformation the profile (projection) can be reversibly decomposed into a large number of sine or cosine waves (Fourier components) of different amplitudes (heights) and frequencies (or wavelengths). These can be plotted on amplitude versus frequency axes. This plot has identical meaning to the original spatial domain curve. Typically the FT of a continuous curve has a continuum of frequencies represented rather than discrete frequencies. Therefore, the Fourier transform provides an alternative means of describing the data. The inverse FT provides an exact reverse process, which simply transforms the data back to the normal activity-time (or distance) axes²⁷.

FT allows the change to an alternative domain where it is more convenient to perform certain operations. For example, the implementation of the convolution operation becomes a simple multiplication performed at each frequency. Though appearing to be more complex than direct convolution, the use of FT can be computationally faster.

4.1.3 Nyquist frequency

In order to preserve a particular frequency in a digital image there must be sufficient sampling. The sampling theorem states that there must be more than two digital samples (measured values or pixels) per cycle of that particular frequency otherwise the frequency is not accurately preserved. The Nyquist frequency is defined as the maximum frequency, which could be recovered with a particular pixel size (in the projections)²⁵:

$$F_N = \frac{0.5}{d}$$

where F_N is Nyquist frequency and d is the pixel size.

The dimension of F_N is typically given in cycles per cm or in cycles per pixel. Aliasing may occur when sampling is too low.

4.1.4 Windows and filters

Since solitary use of ramp filters amplifies the noise (statistical fluctuations) unacceptably, a window function is used to improve the signal-noise (S/N) ratio.

Accordingly practical filters always consist of a ramp filter multiplied by a "low pass" filter or "window". In the frequency domain the window is applied to the ramp filter, this implies that these filters are analogous to actual windows as they are opened up to allow only low frequencies. The cut-off should be the point where the noise predominates and the patient object data are minimal.

The cut-off or critical frequency (f_c) defines the filter shape and beyond this all spatial frequencies in the images are zeroed. Filter order defines the rate at which the filter amplitude falls off. Because high spatial frequencies coincide with those corresponding to statistical noise and because spatial frequencies beyond the Nyquist frequency of the imaging system cannot be visualised, the cut-off spatial frequencies must not exceed the Nyquist frequency⁵⁸.

With the application of a window, noise is reduced. However since sharp edges in the image are also represented by high frequency components, resolution is also compromised by applying filters that "roll off" at high frequencies.

Thus the practical filters always involve a compromise between the extent to which noise must be suppressed and the extent to which resolution deteriorates.

The more noise is suppressed the more the spatial resolution deteriorates and vice versa.

Accordingly a variety of filters are usually available for selection or modification by the operator.

Type of filter used depends on:

- ❖ The counts accumulated (which determines statistical noise content).
- ❖ Resolution of the collimator.
- ❖ Resolution required clinically.

- ❖ Required smoothness, which is the suppression of statistical fluctuations (noise) in the image.

4.1.5 Butterworth filters

These are low pass filters, which due to their flexibility and ease of design have become the filters of choice in most nuclear medicine procedures today⁵⁹. A Butterworth filter, in the frequency (f) domain, is shaped like a curve described by the equation⁵⁹:

$$\text{Butterworth} = \frac{1}{1 + (f / fc)^{2n}}$$

where fc is the critical or cut-off frequency and n is the order of the filter. It can be seen that any Butterworth filter has amplitude of 1 when f is small (low frequencies), amplitude of 0 when f is large (large frequencies) and amplitude of 0.5 when f equals fc . The transition from 1 to 0 can be profoundly modified by acting on the parameters n and fc of the filter. Thus the user has a significant control over the way in which the function falls to zero. The function departs from the ramp filter and falls to zero at a rate controlled by the power factor. The higher the order, the more the window function resembles the rectangular window function.

4.1.6 Filtered backprojection

Frequency domain consists of four steps:

- ❖ Computing the one dimensional FT of each projection.
- ❖ Multiplying the transform by the frequency filter.
- ❖ Computing the inverse FT, yielding the filtered projections.
- ❖ Backprojecting the filtered projections.

4.1.7 Advantages of filtered backprojection

- ❖ Simple and fast.
- ❖ Mathematically exact in the ideal situation.
- ❖ No bias.

4.1.8 Disadvantages of FBP⁶⁰

- ❖ Loss of resolution with filter.
- ❖ Difficulty in choosing filter.
- ❖ It may generate artefacts: mainly stray artefacts and negative values near the border of high activities.

4.2 ITERATIVE RECONSTRUCTION

4.2.1 Introduction

Several iterative approaches have been suggested. What they have in common is an accurate means of estimating the projection data that would be obtained by scanning a hypothetical radionuclide activity distribution contained within a measured or assumed distribution of attenuating material.

Several steps are taken to come up with a reconstructed image:

- ❖ Obtain an estimated or starting image for the iterative process. This is often accomplished by a convolution back projection reconstruction.
- ❖ Data projections are then estimated for this starting image by taking into account attenuation along each projection ray.
- ❖ The difference between these estimated projections and the measured projections are then used to correct the starting image.

The manner in which this difference, or error, is used to change the reconstructed image is the principal difference between various iterative techniques⁶¹.

This entire process, starting with the projected ray sums, is repeated a number of times until an approximate solution within some acceptable criterion of the true result have been reached⁶².

In this thesis, we will focus on maximum likelihood methods, which are based on a statistical measure.

In these methods one tries to find the most probable activity distribution which is consistent with the given data assuming a Poisson distribution as the underlying probability model.

4.2.2 Theoretical background

The reconstruction is based on Bayes' theorem⁶³. The problem is to estimate the activity distribution (act) based on the projections measured by the rotating gamma camera or PET camera. The aim is to find the most likely or probable solution $P(\text{act} | \text{proj})$ given that we have measured the projections. Bayes' theorem states that:

$$P(\text{act} | \text{proj}) \sim P(\text{proj} | \text{act}) \cdot P(\text{act})$$

where:

- ❖ $P(\text{proj} | \text{act})$ is the probability of getting the projection (proj), given an activity distribution (act).
- ❖ $P(\text{act})$ is the priori probability which can encompass prior knowledge about the expected activity distribution.

$P(\text{proj} | \text{act})$ can be calculated for a known activity distribution, provided a reasonable model for the emission of gamma photons and their detection can be assumed.

It can be seen intuitively that reconstruction from the measured projections, that is maximising $P(\text{act} | \text{proj})$, might be achieved by maximising the combination of the modelled estimate of projections and any prior knowledge about the expected reconstruction.

In the absence of prior knowledge this reduces to maximizing $P(\text{act} | \text{proj})$, which can be achieved by minimizing the difference between the estimated projections and the original measured projections.

When the resulting reconstruction is equal to the true activity distribution, then there will be a consistent result where the estimated projections should equal the measured projections.

This makes several assumptions that:

- ❖ There is no noise.
- ❖ The model used to estimate projections includes all factors such as attenuation, distance dependent resolution and object shape dependant scatter.

4.2.3 Maximum likelihood

Likelihood refers to a statistical measure, which is maximized when the difference between estimated and measured projections is minimized when taking the Poisson distribution into account. The most commonly used algorithm is the expectation maximization (MLEM). This involves two steps in tomography:

- ❖ The E-step is to determine the expected projection based on the current estimate of activity.
- ❖ The M-step is to use the difference between the estimated and the measured projections to adjust the current activity distribution so as to be closer to the most likely solution whereby the likelihood is maximized.

This method has the advantage that it can be modified to incorporate⁶⁴:

- ❖ Physical models of attenuation.
- ❖ Full 3-D scatter.
- ❖ Distance dependant detector response including non-standard collimators such as pinhole.
- ❖ The correct noise model.

The method can potentially improve lesion detection⁶⁴.

MLEM is a versatile method, incorporating Poisson statistics in the reconstruction itself.

It converges to a unique solution, albeit slowly.

This slow convergence can be accelerated; the most common accelerator commonly employed being the ordered subset EM (OSEM). This approach is inherently simple⁶³. Instead of modifying all projections per iteration, a subset of projections is used. Progressively using a different subset for each sub-iteration, instead of all projections produces very similar results. This will involve significantly less computations. The surprising thing is that the rate of convergence is almost identical to that using all projections so that the overall speed of reconstruction is significantly reduced.

However it does have its disadvantages:

- ❖ Slow convergence to a final solution, leading to long processing times.
- ❖ Noise will increase at higher iterations and recovery of low frequency is faster than for high frequencies.

❖ Recovery of resolution can be spatially variant.

These disadvantages have led to the conclusion that the “optimal number of iterations is dependant on the specific application and the information sought from a particular image”⁶⁵. Possibly the most clinically compelling evidence that ML reconstruction is useful has been based on very specific clinical examples where reconstruction has been optimized for specific tasks.⁶⁶

CHAPTER 5: METHODS

5.1 Inclusion criteria

Patients were included if the chest radiograph showed a single pulmonary nodule of less than 6 cm completely surrounded by parenchymal lung tissue with or without hilar or mediastinal lymphadenopathy. Follow-up included chest CT, bronchoscopy and either thoracotomy, fine needle aspiration cytology or repeated CXR documentation over two years. Histological, cytological or microbiological data were obtained to establish final diagnosis and in cases where no histology was done, a follow-up chest radiograph was used to diagnose benignity.

The patients still on follow up for two years were included in this study. Of note is that follow up for two years is done if the history and anatomic imaging are highly suggestive of a benign lesion. Some patients were classified as having an unknown diagnosis as the follow up period had not been completed.

These patients were then studied with Tc-99m MIBI and Tl-201. Both studies were performed on the same day, with the thallium study carried out before the MIBI study. Planar views and single photon emission computed tomography (SPECT) of the chest area were obtained before any definitive diagnosis procedure.

5.2 Image acquisition

5.2.1 Tl-201

Patients were injected with 160 MBq of Tl-201 in a foot vein or arm vein contralateral to the side of the lesion and images were taken at 10 minutes post-injection. Planar and tomographic imaging began 10 minutes after injection. A dual headed Elscint Helix gamma camera was used equipped with low energy, all purpose (LEAP) collimators. The energy windows were set at 15% and the peak energy of the X-ray photons was used (69-

83 KeV). For the planar images anterior, posterior and lateral views were taken, each over 300 seconds.

For SPECT the Tygerberg Hospital Nuclear Medicine Department routine protocol was used:

- ❖ Rotation of the gamma camera head over an angle of 360 degrees.
- ❖ Step and shoot mode of 3 degrees per step, acquisition time of 15 seconds.
- ❖ Use of a non circular orbit.
- ❖ Image matrix used: 64 x 64 pixels.

5.2.2 Tc-99m MIBI

Patients were injected with 760 MBq of Tc-99m MIBI in the foot vein or arm vein contralateral to the lung lesion. The same acquisition protocol was used, however 10% of the photopeak of 140 keV was set.

5.3 Image Reconstruction

Both filtered backprojection (FBP) and OSEM (ordered subsets expectation maximisation) iterative reconstruction were used to reconstruct images. For filtered backprojection, data was first filtered with a Butterworth filter having a cutoff frequency of 0.8/cm and an order of 6. Transverse slices were reconstructed and from these, coronal and sagittal slices were produced.

For OSEM, images were reconstructed using 8 subsets with 6 iterations. Post reconstruction, 3-dimensional filtering was done using a Butterworth filter, cutoff 0.6/cm and of the order 3. The same image position and number of slices was maintained with each algorithm to enable co-registration. No zooming was applied during the processing of images. The filter parameters were optimised for image quality.

5.4 Image analysis

Transverse, coronal and sagittal slices were displayed with a grey scale. Image co-registration was done using the multimodality system on the HERMES to enable more accurate comparison of the images produced by iterative reconstruction and those done by FBP. Images reconstructed using OSEM were maintained on the left side of the screen and those from FBP on the right side. The x, y, z planes were adjusted on the OSEM images and copied onto the FBP images.

Depending on the best view used to locate the lesion on the chest radiograph, a corresponding view of the tomograph was used. For example, if the lesion was best seen on the posterior-anterior view then coronal sections were used and if best seen on the lateral view then sagittal views were used. Coronal views were used for most patients.

A region of interest was drawn outside the outer border of the lesion on the OSEM images and this was automatically mirrored on the FBP image. For the background one of the following options were used:

- Automatic horizontal mirror (contralateral side).
- Automatic vertical mirror (ipsilateral side).
- Manual horizontal mirror (contralateral side).
- Manual vertical mirror (ipsilateral side).

The signal to noise ratio (SNR) was chosen as a measure to show the effect of reconstruction on lesion detection. Image noise may be appraised by evaluating the relationship between noise and target, where noise is the standard deviation of the background. It is important to note that the SNR is considerably less in tomographic than conventional imaging for the same number of counts. An approximate rule of thumb is that to obtain the same statistical accuracy (SNR) in tomography about five times as many counts need to be collected as SPECT is particularly photon deficient⁶⁷. It has been shown that improved noise property and better image quality yielded by iterative reconstruction has the potential to improve the detection of smaller lesions⁶⁸.

The term signal was used in image processing to denote the ideal, uncorrupted state of the image, where each pixel represents the "true mean"⁶⁹. Noise is considered as the statistical variation from the "true mean" in each pixel. This leads to the concept of the

signal to noise ratio, which refers to the relative power of the signal and noise either overall or at a given frequency.

The following formula was used:

$$\text{SNR} = \frac{\text{Mean counts ROI(lesion)} - \text{Mean counts background}}{\text{Standard deviation background}}$$

The target to background ratio (T/B ratio) was also calculated:

$$\text{T/B ratio} = \frac{\text{Mean counts ROI(lesion)}}{\text{Mean counts background}}$$

Both SNR and T/B ratio can be used in a clinical evaluation, i.e. differentiation between malignant and benign lesions.

The effect of iterative versus filtered backprojection reconstruction will be analyzed as sensitivity, specificity and accuracy in reference to single pulmonary nodule diagnosis. No emphasis is put on the difference between Tl-201 and Tc-99m MIBI in terms of their diagnostic ability.

5.5 Data analysis

Assessment of the diagnostic performance is being done using sensitivity and specificity.

Results of the diagnostic performance of OSEM and FBP are classified as:

- ❖ True positives (TP)
- ❖ False negative (FN)
- ❖ True negative (TN)
- ❖ False positive (FP)

in reference to the final diagnosis based on the gold standard. For a given cutoff or decision threshold value, defined for both SNR and T/B ratios, a result is classified as ‘positive’ if above this or ‘negative’ if below. Sensitivity and specificity are then calculated as:

$$\begin{aligned}\text{Sensitivity} &= \frac{\text{true positives}}{\text{actual positives}} \\ &= \frac{\text{TP}}{\text{TP} + \text{FN}}\end{aligned}$$

$$\begin{aligned}\text{Specificity} &= \frac{\text{true negative}}{\text{actual negative}} \\ &= \frac{\text{TN}}{\text{TN} + \text{FP}}\end{aligned}$$

Sensitivity represents the accuracy of the algorithm in identifying the actually positive cases and specificity represents the accuracy of identifying the actually negative cases.

Receiver operating characteristics (ROC) curves were then generated by varying the cut-off or decision threshold. This involved recalculating sensitivity and specificity of each algorithm at each threshold that was used. To construct the ROC curve the x-axis is 1 minus the specificity (false positive rate) and the y-axis is sensitivity (true positive rate). The ROC curves will show the trade-off between the sensitivity and the specificity as we vary the decision threshold.

The area under the ROC curve (AUC) can be calculated either by using a non-parametric method based on constructing trapezoids under the curve as an approximation of the area or a parametric method using a maximum likelihood estimator to fit a smooth curve to the data points. In this study the area under the curve was calculated using GRAPHROC. The standard error calculation was based on the equation used by Hanley et al.⁷⁰ and a z-statistics was used to assess the difference between the AUC of the paired data. In another study, Hanley et al.⁷¹ considered a specific case of randomly paired normal and abnormal radiological images and showed that the area under the ROC curves is a measure of the probability that the perceived abnormality of the two images will allow correct identification. Accuracy then can be measured using the area under the ROC curve that is the ability to correctly classify those with and without the disease under investigation.

Interpretation of the ROC curves will enable accurate comparison of the effect of OSEM and FBP on the diagnosis of single pulmonary nodules.

CHAPTER 6: RESULTS

6.1 Patients

A total number of 33 patients were studied, 19 men and 14 women. The age range was wide (20-90 years) with a median age of 57 years.

Table 6.1 shows the patient clinical data including the final diagnosis. The patients were grouped according to their final diagnosis. The diagnosis of four patients was classified as unknown since these patients are still being followed up for two years on the basis of their chest X-ray and CT findings which were considered suggestive of benignity.

6.2 Studies

A total of 25 Tl-201 studies and 33 Tc-99m MIBI studies were done but only 32 studies from the latter could be processed because data could not be found for one study (figure 6.1).

All the studies available were processed using both OSEM and FBP. A region of interest was drawn outside the outer border of the lesion on the OSEM images and this was automatically mirrored on the FBP image. For the background, automatic horizontal mirroring was used in 18 patients, first done on the OSEM images and automatically copied onto the FBP images. For those cases where automatic horizontal mirroring resulted in selection of a visibly hot background, (over the heart or over the liver), automatic vertical mirroring was used (4 patients). If the latter still resulted in a hotter background, then manual vertical mirroring was done (11 patients). A hot background was defined as one whose counts are higher than those of the region of interest (lesion). Manual vertical mirroring resulted then in biased background selection.

Detection was found to be the same for both algorithms. All the malignant nodules were detected when using either of the two radiopharmaceuticals and when using either of the two reconstruction algorithms. The detection ability was different for the two radiopharmaceuticals in relation to the type of single pulmonary nodule as illustrated by figure 6.1. Of note is that Tl-201 detected more tuberculosis nodules in comparison to Tc-99m MIBI.

Pt	Age	Gender	Lobe	Lesion Size (cm)	Additional Clinical Data	FD	Tl-201	Tc-99m MIBI	Comment
1	37	Male	Left lower	2	Left lobe resection TB	B	1	1	
2	65	Male	Right mid	0.5	Bronchoscopy negative, stable size for 2 years	B	0	0	near liver
3	29	Female	Left lower	0.8	No double on CT, had TB as a child	B	0	1	near heart
4	58	Female	Left lower	2	Histology-Ziehl Nielsen stain negative	B	0	0	near liver
5	43	Male	Right upper	1.7	Bronchoscopy negative. No surgery	B	1	0	
6	44	Male	Right upper	2.5	Follow up for 2 years, no change in size	B	0	1	
7	56	Female	Left upper	2	SPN decreasing in size on follow up	B	0	0	near heart
8	46	Female	Right mid	2	Lesion size decreasing on follow up	B	ND	1	
9	57	Male	Left lower	2.5	Histocytology-Haemophilus influenza	B	1	0	near heart
10	61	Male	Right lower		Stable lesion in 2 years, calcified	B	1	1	
11	48	Female	Left upper	2	Post TB for follow-up	B	ND	1	
12	62	Male	Right mid		Haemophilus influenza seen	B	1	0	near heart
13	53	Female	Left upper	1	Histology - benign	B	0	0	
14	61	Male	Left hilar	1	Histo-Adenocarcinoma with lymph node	M	1	NA	
15	60	Female	Right lower	2	Histo-adenocarcinoma, poorly differentiated	M	1	1	near heart
16	63	Male	Right lower	1.2	Histology-squamous cell ca, poorly differentiated	M	1	1	near heart
17	90	Male	Right upper		Massive lesion, malignant	M	1	1	
18	72	Female	Right upper		Histology- adenocarcinoma with right hilar nodes	M	1	1	
19	67	Male	Right lower	2.5	Squamous cell carcinoma, complete excision	M	1	1	
20	68	Male	Right hilum		Metastatic adenocarcinoma, incomplete excision	M	ND	1	
21	72	Male	Right hilum	1.5	Histology - Right lymphoma node	M	ND	1	
22	52	Male	Right upper	4	Histology-TB granuloma	TB	0	1	
23	49	Male	left apex	3	Histology- TB granuloma	TB	1	0	
24	44	Female	Right upper		Histology- Active TB	TB	1	0	
25	29	Female	Right upper	2	Histology: tuberculosis on treatment	TB	1	0	near heart
26	57	Male	Right upper	2	Histology-caseating granuloma	TB	0	1	
27	36	Female	Left lower	5	Previous TB, pneumonectomy for bronchiectasis	TB	1	1	near vertebrae
28	35	Male	Left lower	2	Histology-TB scar	TB	1	0	near heart
29	63	Female	Right upper	1.6	Histology TB	TB	1	1	
30	57	Male	Left upper	2.1	Being followed up for 2 years	U	ND	1	
31	72	Male	Left lower		Refused operation, suggestive of malignancy	U	ND	1	
32	20	Female	Right upper		Systemic sclerosis for follow up	U	ND	1	
33	67	Female	Right upper	3	Unknown	U	ND	1	

Table 6.1: clinical data of all patients. Abbreviations used: Pt: patient; FD: final diagnosis; B: benign, M: malignant, TB: tuberculosis, U: unknown; ND: not done; NA: not available. 0 means no lesion detected and 1 stands for the detected SPN.

6.3 SNR and T/B ratio

Semi-quantitative analysis was done using signal-to-noise ratio (SNR) and tumour-to-background (T/B) ratio. Results are shown in table 6.2 and figure 6.2, 6.3, 6.4 and 6.5. There seems to be more improvement in SNR and T/B ratios with OSEM for both the Tl-201 (9/17) and Tc-99m MIBI (14/21) images. Higher values with FBP can however be seen and interestingly several of these are when the lesion is close to a 'hot' background like for example heart, liver or vertebrae.

In this analysis, patients with tuberculosis and those with unknown final diagnosis were excluded. The former were excluded due to the high uptake of Tl-201 by tuberculosis nodules which made differentiation from malignant nodules difficult and therefore increased the risk of false positives. Sensitivities and specificities were calculated at each threshold for the two algorithms and plotted as two separate graphs (Figures 6.6 – 6.9). Initially graphs were drawn to show the difference in sensitivity and specificity at different thresholds.

Figure 6.6 (upper panel) shows graphs obtained for the Tl-201 studies using SNR thresholds. OSEM generally shows higher sensitivity and specificity for most thresholds. For example, at the SNR threshold of 2.0, OSEM has a sensitivity and specificity of 65% and 90% respectively. In comparison, FBP has a sensitivity of 30% and specificity of 70% at the same threshold. At higher thresholds (SNR greater than 3.0) the two algorithms appear to perform equally in terms of sensitivity and specificity for example at SNR threshold of 3, both have a low sensitivity of 18% and high specificity of 100%.

With Tc-99m MIBI studies (Figure 6.6 lower panel) the difference between the OSEM and FBP is less pronounced. Again OSEM has higher values at the same thresholds. For example at SNR threshold of 2.0, OSEM has a sensitivity of about 40% and specificity of 75%. At the same threshold, FBP shows a sensitivity and specificity of 28% and 75% respectively. At low SNR the two reconstruction algorithms perform equally. For example, at SNR 1.0, both have a sensitivity of 85% and a specificity of 75%.

Using T/B ratios in the analysis of the Tl-201 studies, a similar pattern is seen to that with SNR (figure 6.7 upper panel). There is improved performance of OSEM. For example at T/B ratio threshold of 1.5, OSEM has a sensitivity of 65% and a specificity of 90% in comparison to FBP which has sensitivity and specificity of 50% and 60% respectively. At higher thresholds, FBP performs better: for example at threshold 2.0, OSEM has a sensitivity of 15% in comparison to 30% for FBP whilst specificity is 100%.

Pt	FD	detection TI-201	SNR	SNR	T/B	T/B	detection Tc-99m MIBI	SNR	SNR	T/B	T/B
			OSEM TI-201	FBP TI-201	OSEM TI-201	FBP TI-201		OSEM Tc-99m MIBI	FBP Tc-99m MIBI	OSEM Tc-99m MIBI	FBP Tc-99m MIBI
1	B	1	0.91	0.56	1.3	1.2	1	1.96	2.14	1.2	1.2
2	B	0					0				
3	B	0					1	1.29	1.13	1.6	1.4
4	B	0					0				
5	B	1	0.65	0.49	1.1	1.2	0				
6	B	0					1	0.48	0.35	1.1	1.1
7	B	0					0				
8	B	ND					1	0.67	0.49	1.2	1.2
9	B	1	1.33	2.5	1.4	1.6	0				
10	B	1	2.57	1.84	1.6	1.6	1	2.01	2.13	1.8	1.9
11	B	ND					1	3.52	3.97	1.5	1.6
12	B	1	1.29	2.85	1.2	1.6	0				
13	B	0					0				
14	M	1	0.48	0.43	1.2	1.2	NA				
15	M	1	2.40	2.19	1.5	1.4	1	3.85	2.32	2.3	2.0
16	M	1	0.92	1.12	1.9	2.1	1	1.70	1.45	1.7	1.8
17	M	1	2.82	3.88	2.2	2.4	1	1.88	1.82	2.1	2.4
18	M	1	5.63	2,00	1.2	1.2	1	0.12	0.08	1.0	1.0
19	M	1	2.37	0.33	1.6	1.6	1	1.35	1.18	1.3	1.3
20	M	ND					1	2.66	2.47	1.7	1.6
21	M	ND					1	2.13	1.81	1.4	1.4
22	TB	0					1	0.76	0.47	1.2	1.2
23	TB	1	0.47	0.43	1.1	1.1	0				
24	TB	1	0.36	0.45	1.2	1.3	0				
25	TB	1	1.45	0.6	1.5	1.2	0				
26	TB	0					1	0.75	0.54	1.4	1.2
27	TB	1	2.69	2.84	1.7	1.8	1	2.59	2.87	1.8	1.7
28	TB	1	3.64	4.82	2.3	2.1	0				
29	TB	1	3.52	3.97	1.5	1.6	1	2.58	3.41	1.5	1.5
30	U	ND					1	5.69	4.59	2.0	1.7
31	U	ND					1	5.24	5.48	2.4	3.0
32	U	ND					1	2.00	1.71	1.2	1.2
33	U	ND					1	5.00	4.55	1.6	1.7

Table 6.2: SNR and T/B ratio. Same abbreviations as in table 6.1.

With Tc-99m MIBI studies, the two algorithms perform similarly at almost all the thresholds when using T/B ratio (figure 6.7B). This pattern is again similar to that seen using SNR thresholds. For example at T/B ratio threshold of 1.5 both OSEM and FBP have the same sensitivity of 58% and specificities of 75% and 85% respectively. FBP

then appears to behave better for a short threshold interval after which OSEM improves again. The overall performance of the two reconstruction algorithms at higher thresholds is equal.

Since uptake in the tuberculosis nodules is similar to that in the malignant nodules, tuberculosis resulted in false positives in this study. The effect of OSEM and FBP on the positive fraction (within the group with tuberculosis nodules) at different SNR and T/B ratio threshold is studied in figures 6.8 and 6.9. Tl-201 has a higher maximum fraction of positive cases (75%) in comparison to Tc-99m MIBI (50%) when detection is done visually. Figures 6.8 and 6.9 show that when using Tl-201 or Tc-99m MIBI, FBP initially has a lower fraction of positives at lower thresholds in comparison to OSEM. For example (figure 6.9 upper panel) at a T/B ratio threshold of 1.5, OSEM results in 50% positives for Tl-201 whilst FBP results in 40%. At higher thresholds this is reversed: for example, at a threshold of 1.7, FBP has a fraction of 22% for Tl-201 in comparison to 10% for OSEM.

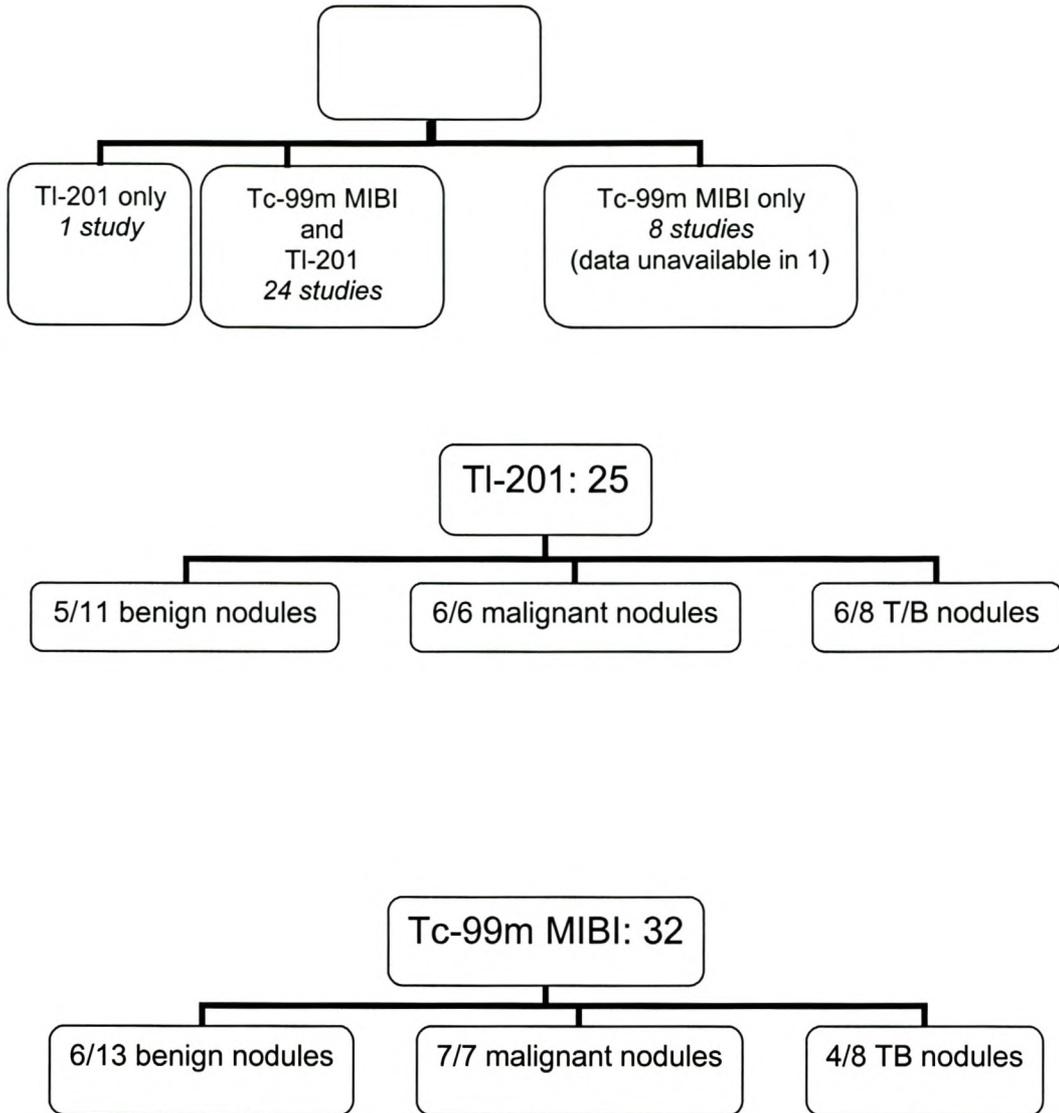


Figure 6.1: Overview of the studies performed. Top panel: relation with type of imaging. Middle panel: Relation of the TI-201 studies with final diagnosis, that is the number of nodules detected for each diagnosis by TI-201. Bottom panel: Relation of the MIBI studies with final diagnosis, that is the number of nodules detected by MIBI for each diagnosis.

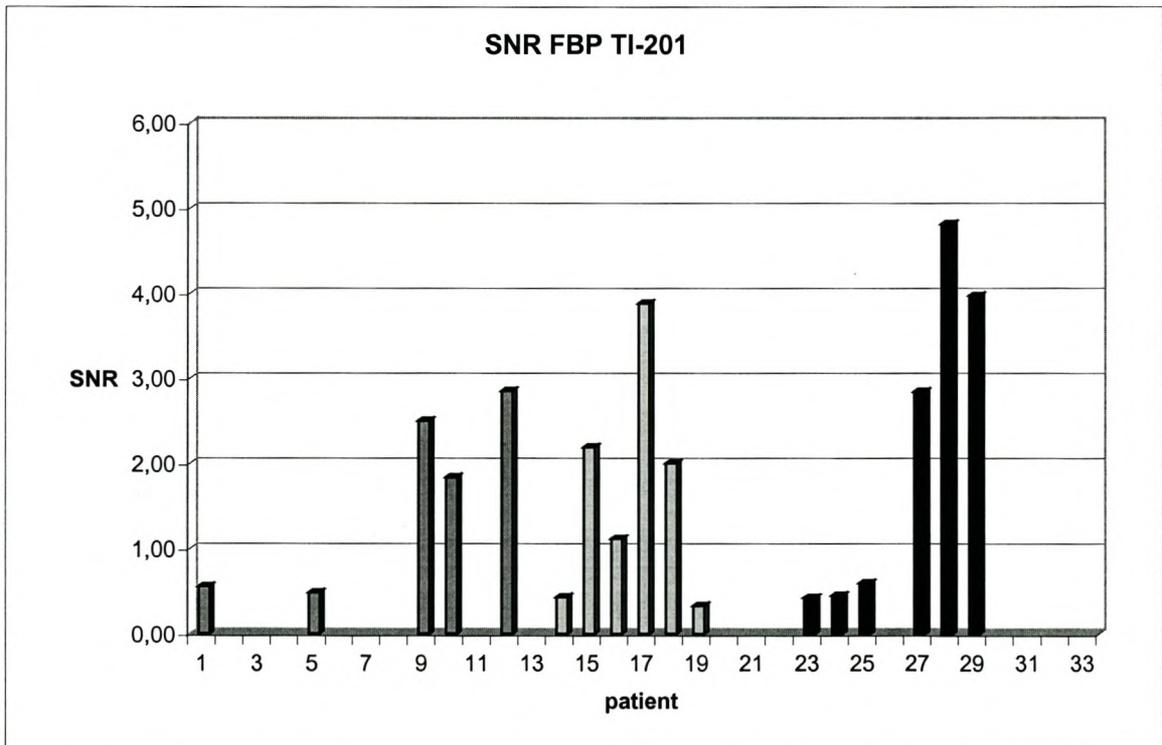
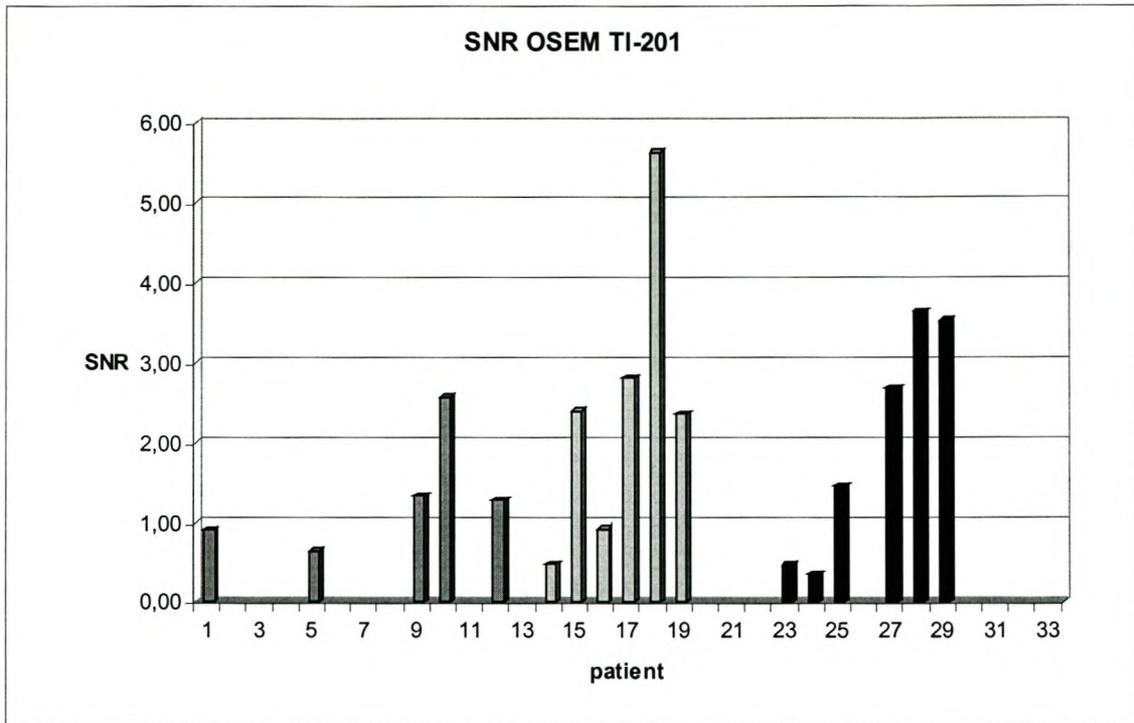


Figure 6.2 showing the SNR for OSEM (upper panel) and FBP (lower panel) in the case of TI-201. Colour coding: dark grey: benign SPN, light grey: malignant SPN, black: tuberculosis, white: unknown final diagnosis.

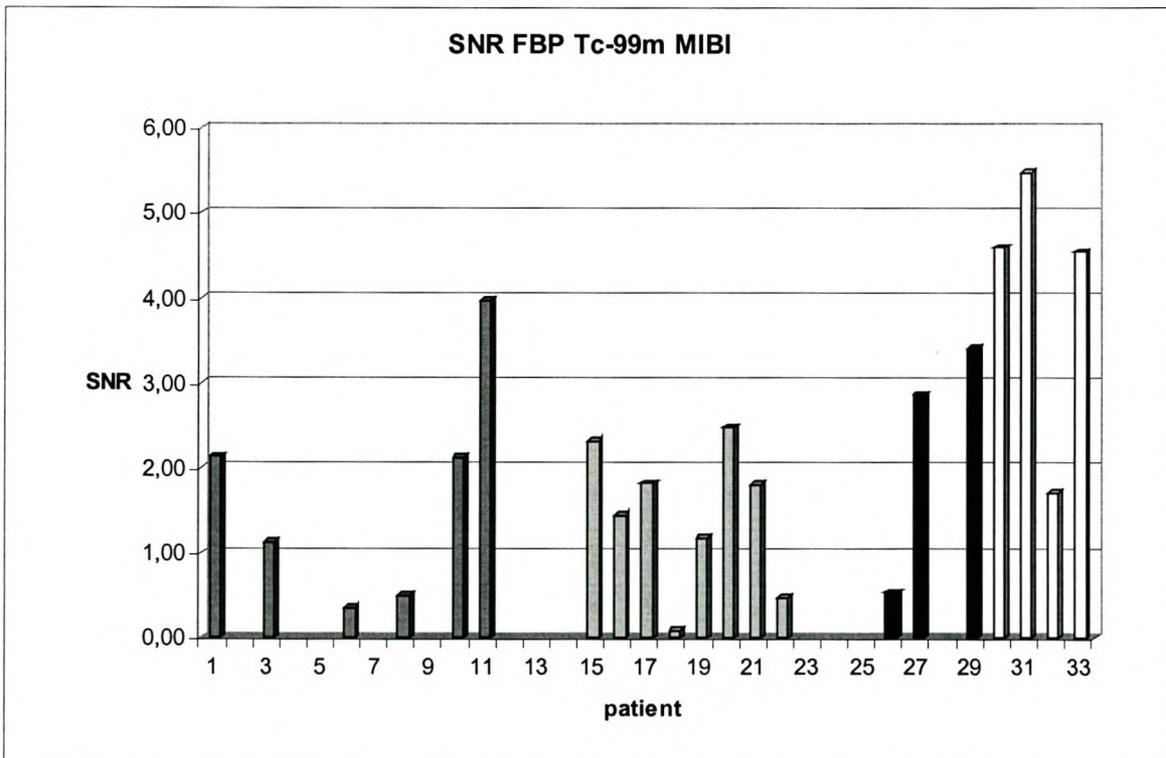
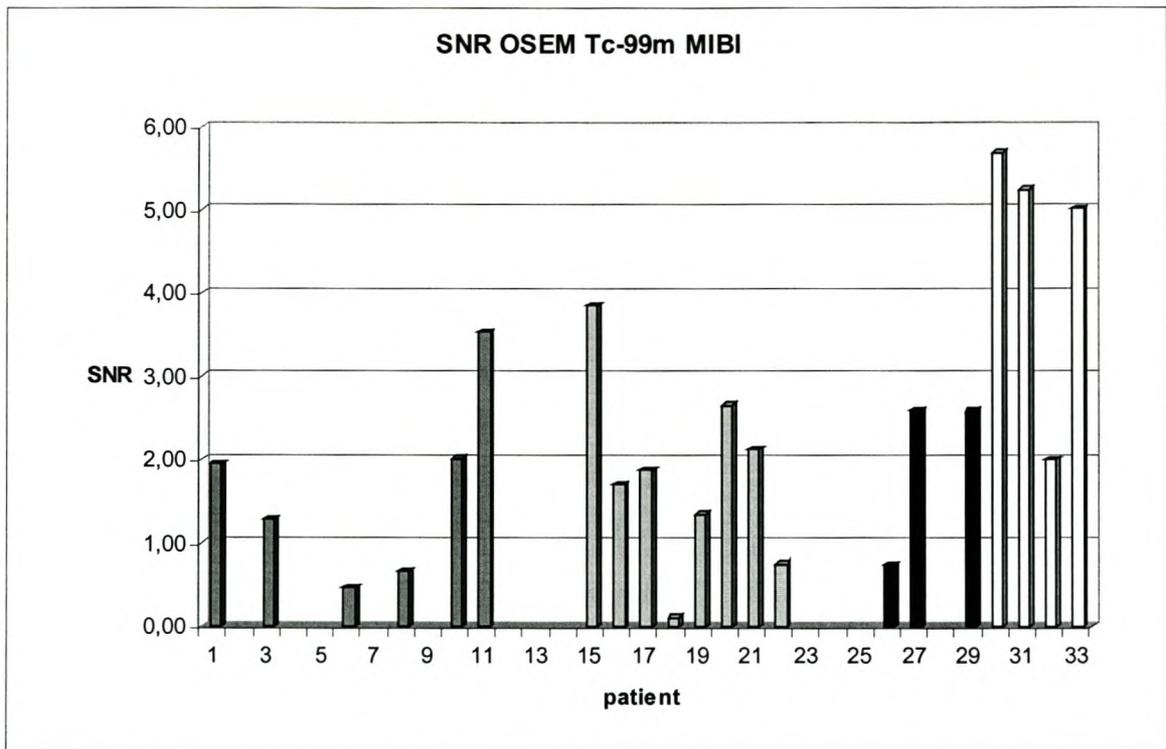


Figure 6.3 showing the SNR for OSEM (upper panel) and FBP (lower panel) in the case of Tc-99m MIBI. Colour coding: same conventions as in figure 6.2.

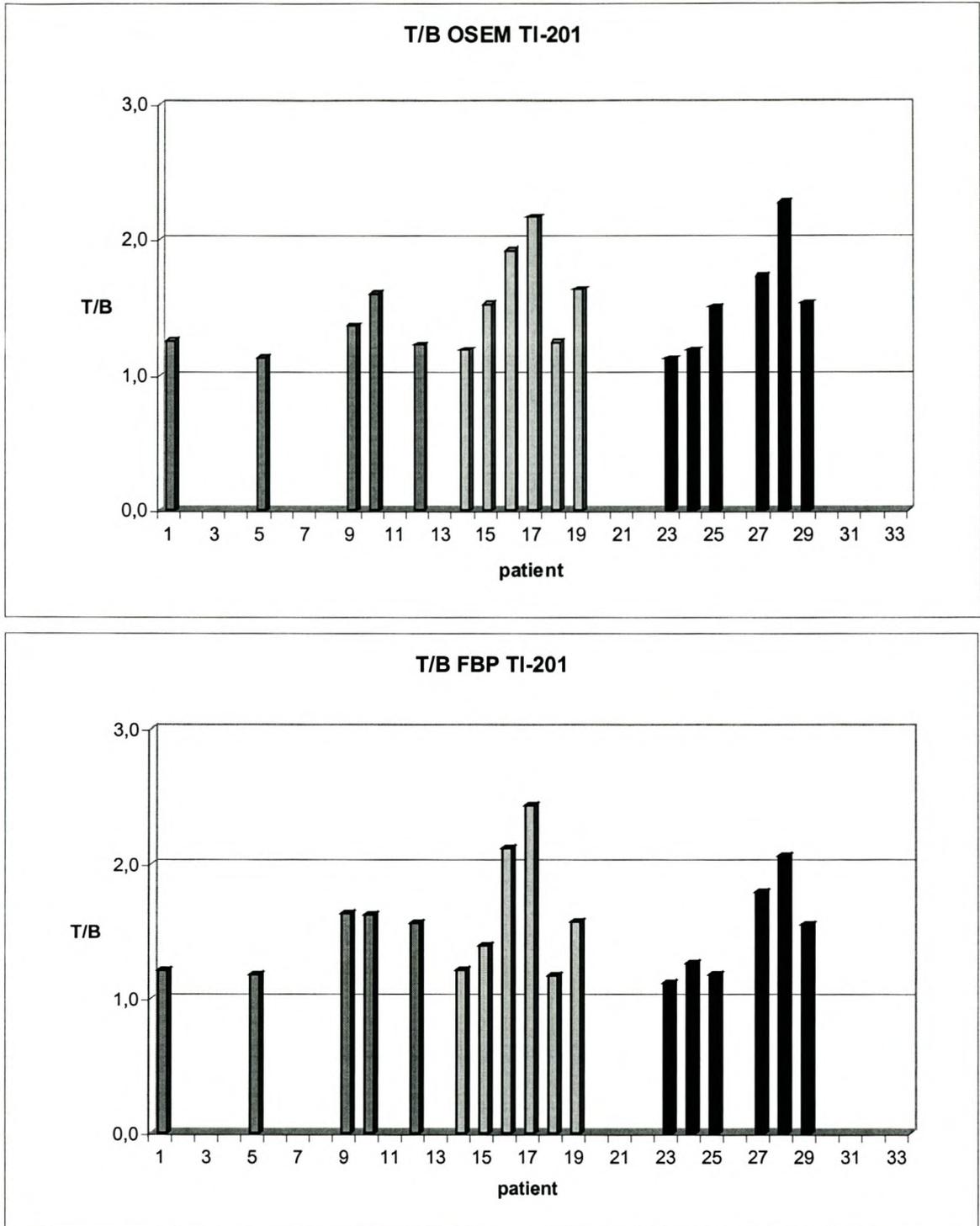


Figure 6.4 showing the T/B ratio for OSEM (upper panel) and FBP (lower panel) in the case of TI-201. Colour coding: same conventions as in figure 6.2.

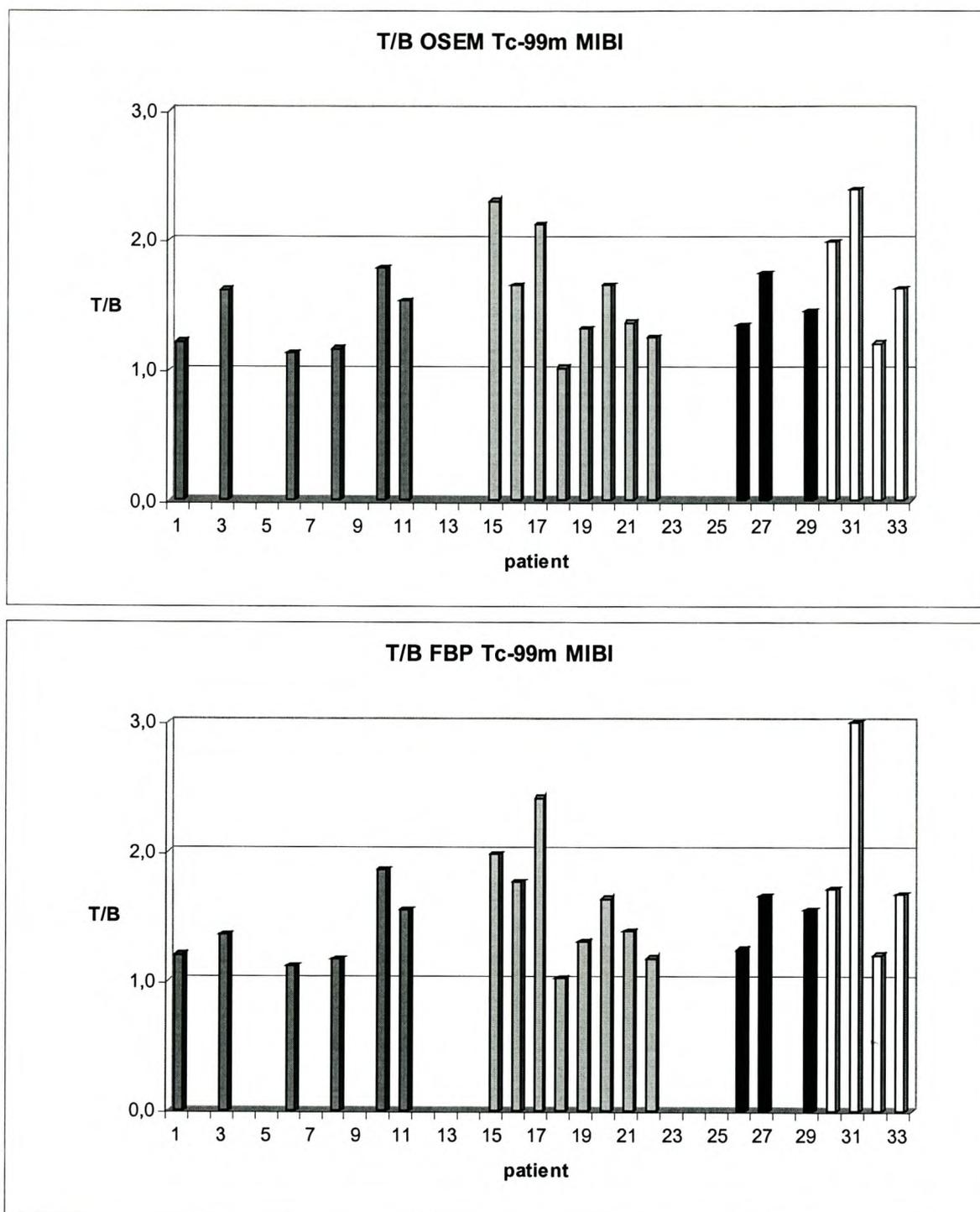


Figure 6.5 showing the T/B ratio for OSEM (upper panel) and FBP (lower panel) in the case of Tc-99m MIBI. Colour coding: same conventions as in figure 6.2.

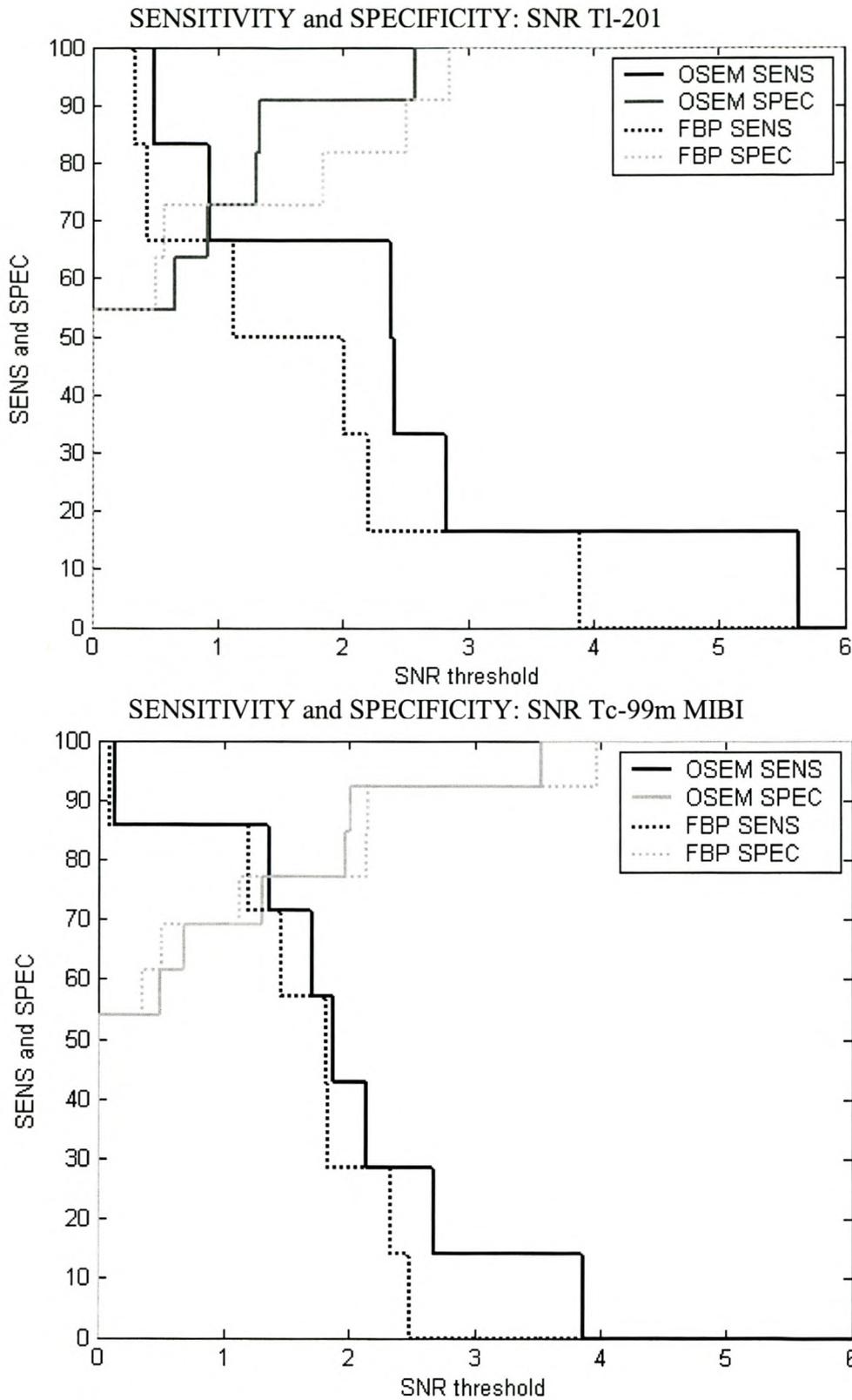


Figure 6.6 shows the sensitivity (black) and specificity (grey) for OSEM (full line) and FBP (dashed line) in the case of Tl-201 (upper panel) and Tc-99m MIBI (lower panel) using the SNR as threshold.

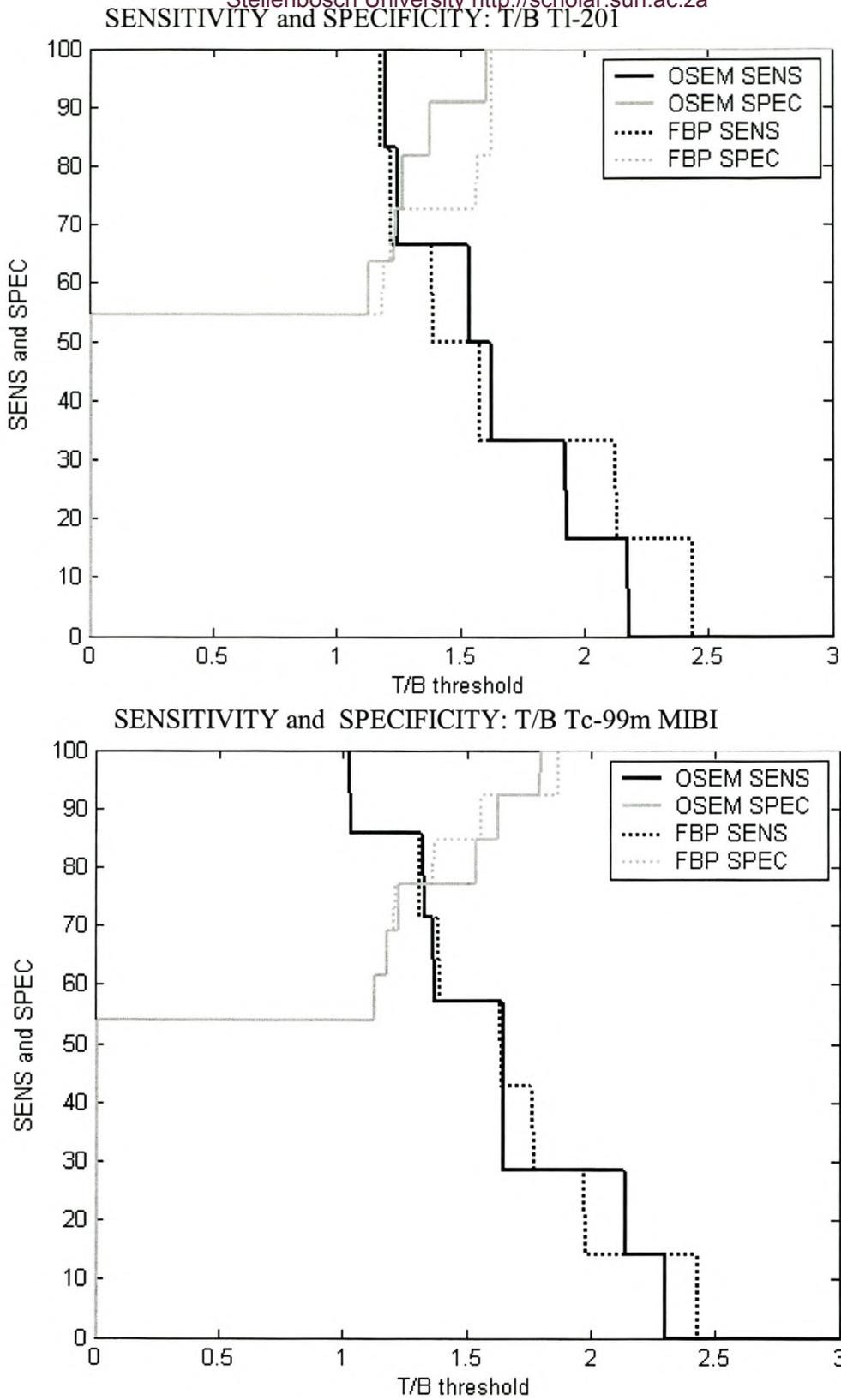
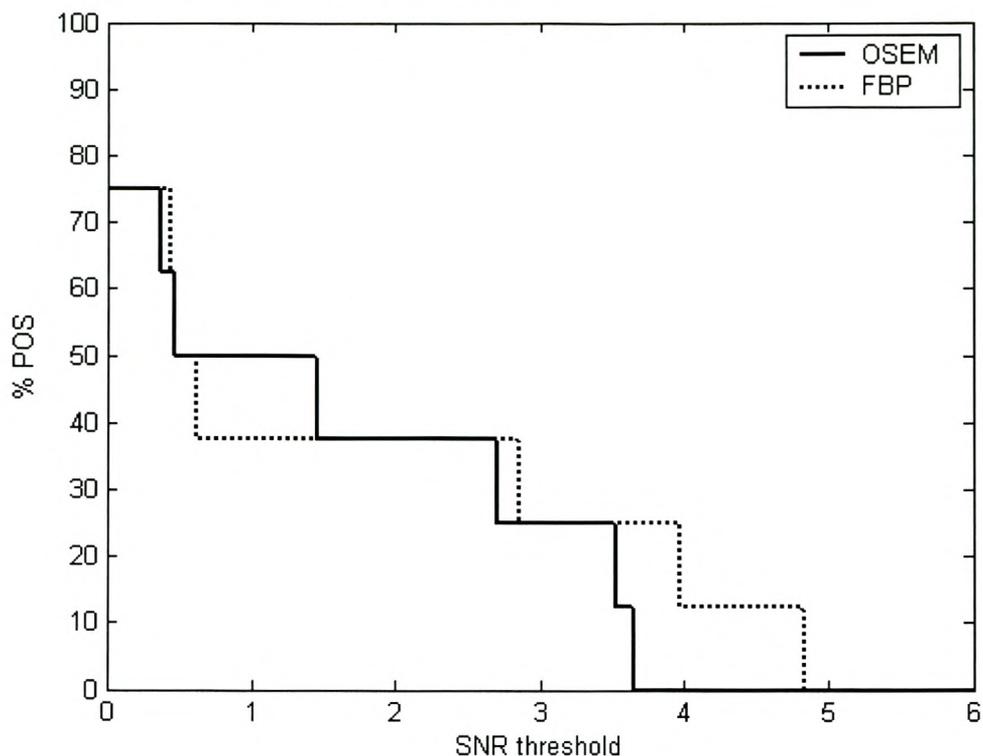


Figure 6.7 shows the sensitivity (black) and specificity (grey) for OSEM (full line) and FBP (dashed line) in the case of Tl-201 (upper panel) and Tc-99m MIBI (lower panel) using the T/B ratio as threshold.

Tuberculosis cases: SNR Tl-201



Tuberculosis cases: SNR Tc-99m MIBI

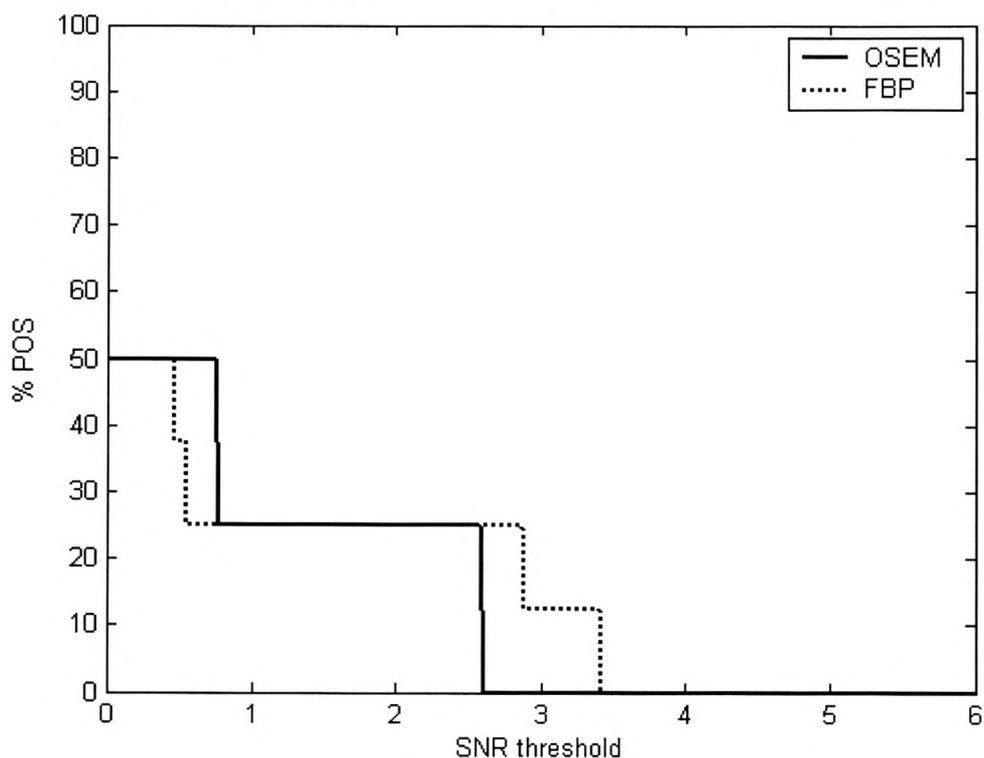
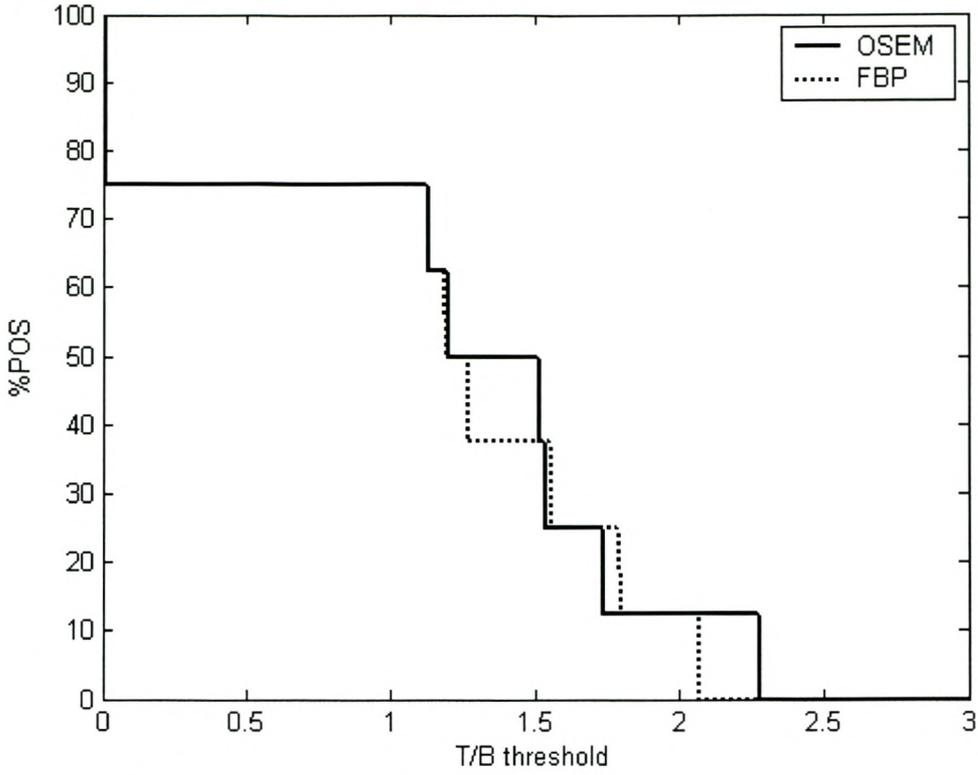


Figure 6.8 shows the percentage positive scored tuberculosis cases for OSEM (full line) and FBP (dashed line) in the case of Tl-201 (upper panel) and Tc-99m MIBI (lower panel) using the SNR as threshold.



Tuberculosis cases: T/B Tc-99m MIBI

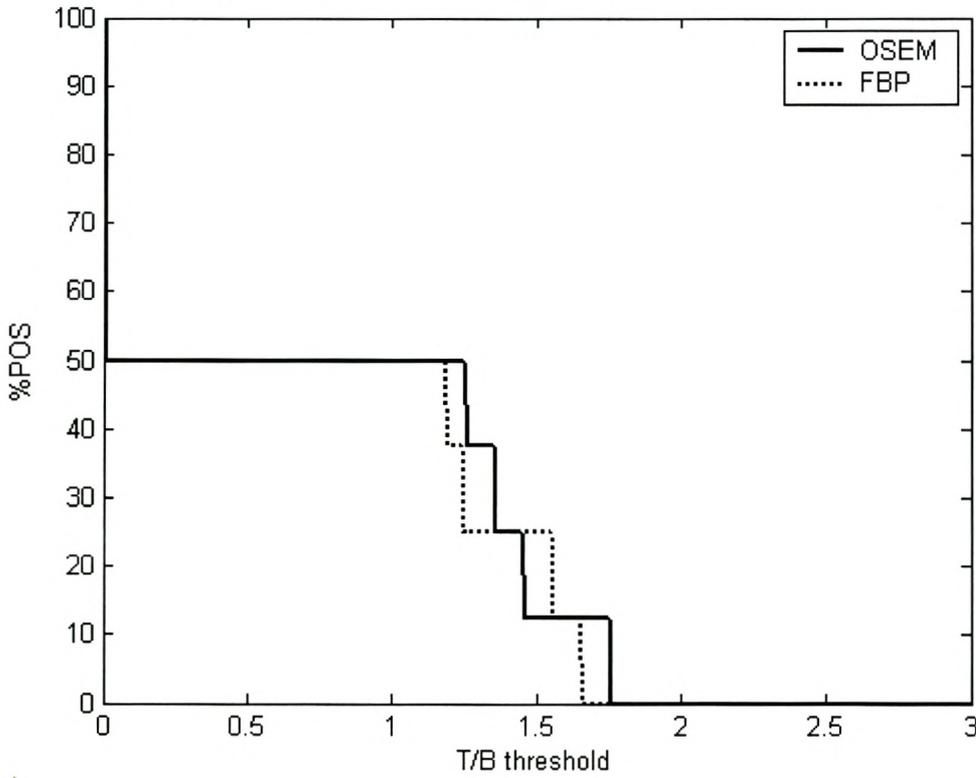


Figure 6.9 shows the percentage positive scored tuberculosis cases for OSEM (full line) and FBP (dashed line) in the case of Tl-201 (upper panel) and Tc-99m MIBI (lower panel) using the T/B ratio as threshold.

6.4 ROC analysis

Receiver operating characteristic curves were drawn by changing the threshold for SNR and T/B ratios for both OSEM and FBP. This gives an idea of the overall performance by looking at the ROC curves in figures 6.10 and 6.11. The closer the curve follows the left hand border and then the top border of the ROC space the more accurate the test. Using SNR, a clear difference can be seen between the ROC curves of OSEM and FBP for Tl-201 (Figure 6.10 upper panel). From this, it can be seen that using Tl-201, OSEM is more accurate at differentiating malignant from benign SPNs than FBP in this study.

When Tc-99m MIBI is used, the reconstruction algorithms are seen to perform equally at almost all SNR thresholds (figure 6.10 lower panel). The same general trend is seen using T/B ratio as the threshold (figure 6.11).

The areas under the curve (AUC), including standard error, for Tl-201 were: OSEM 0.84 +/- 0.11 and FBP 0.74 +/- 0.12 using SNR. A paired test showed that $p = 0.1$. Using T/B ratios the AUC is: OSEM 0.87 +/- 0.14 and FBP 0.78 +/- 0.10 and $p = 0.21$.

For the Tc-99m MIBI studies, using SNR thresholds AUC is: OSEM 0.81 +/- 0.11 and FBP 0.78 +/- 0.11 and $p = 0.62$. Using T/B thresholds AUC is: OSEM 0.85 +/- 0.09 and FBP 0.85 +/- 0.1 and $p = 0.91$. The p value for the Tc-99m MIBI values are much higher and of note is that using the T/B ratios the algorithms have an equal AUC value.

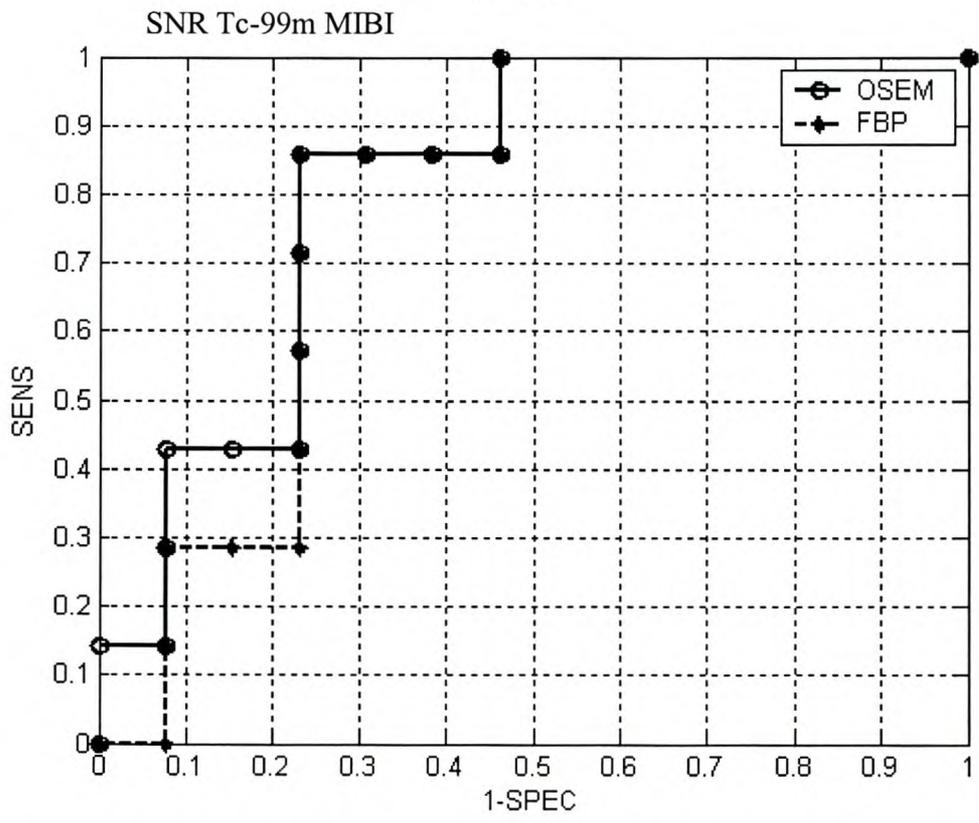
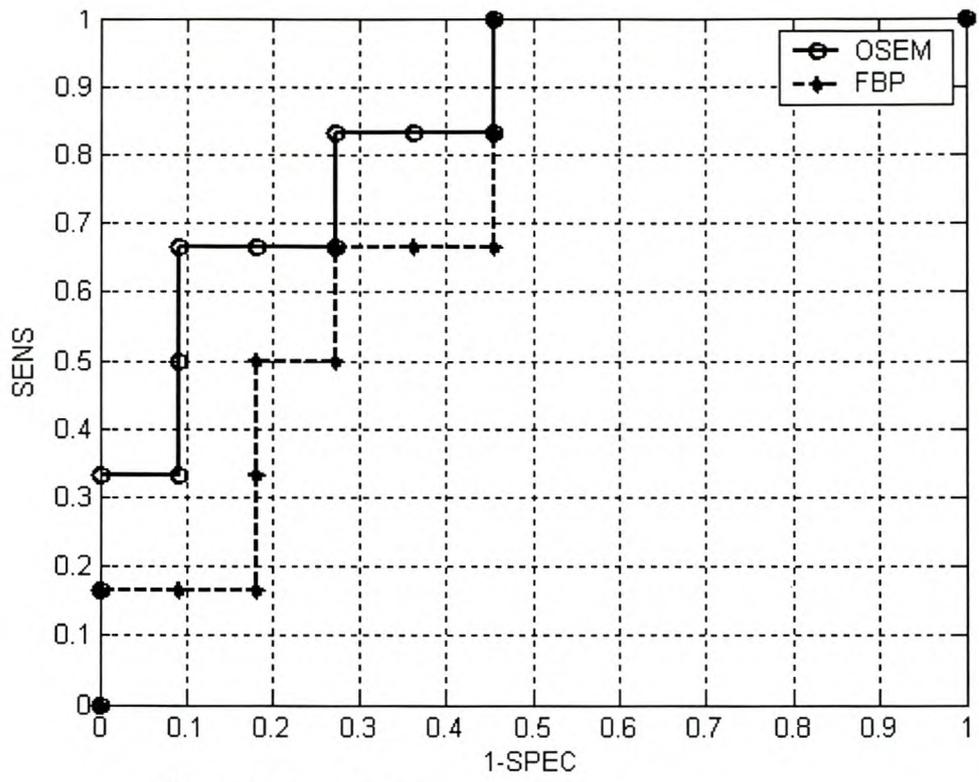


Figure 6.10 shows the ROC curves for OSEM (full line) and FBP (dashed line) in the case of Tl-201 (upper panel) and Tc-99m MIBI (lower panel) using the SNR as threshold.

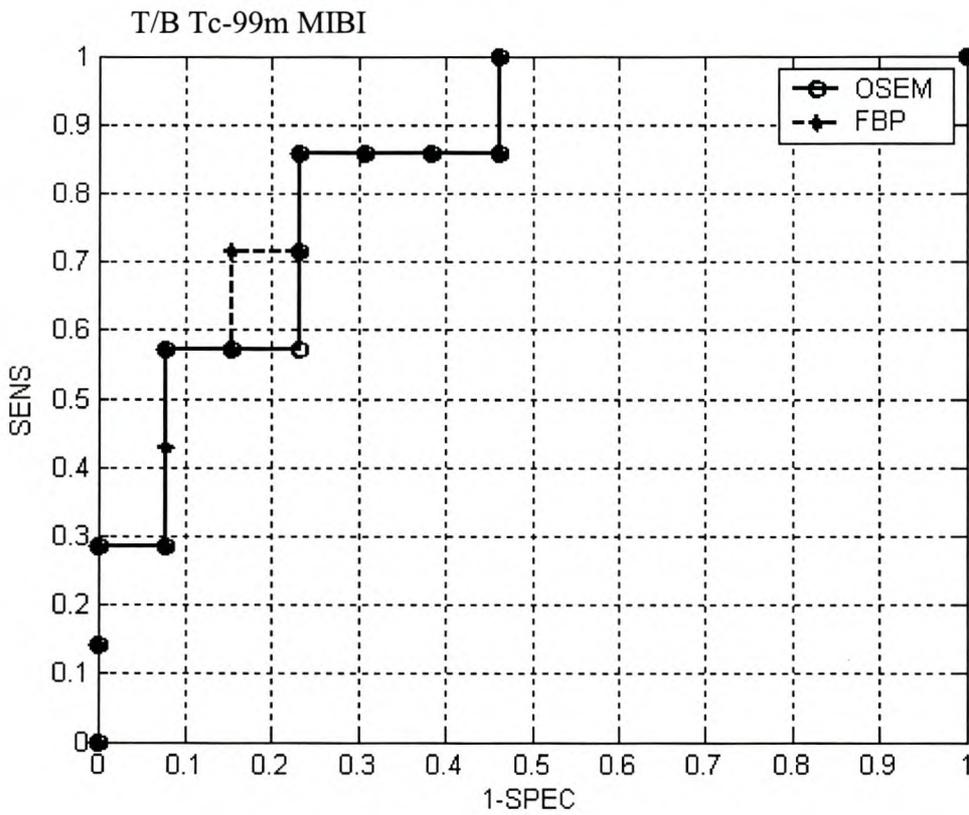
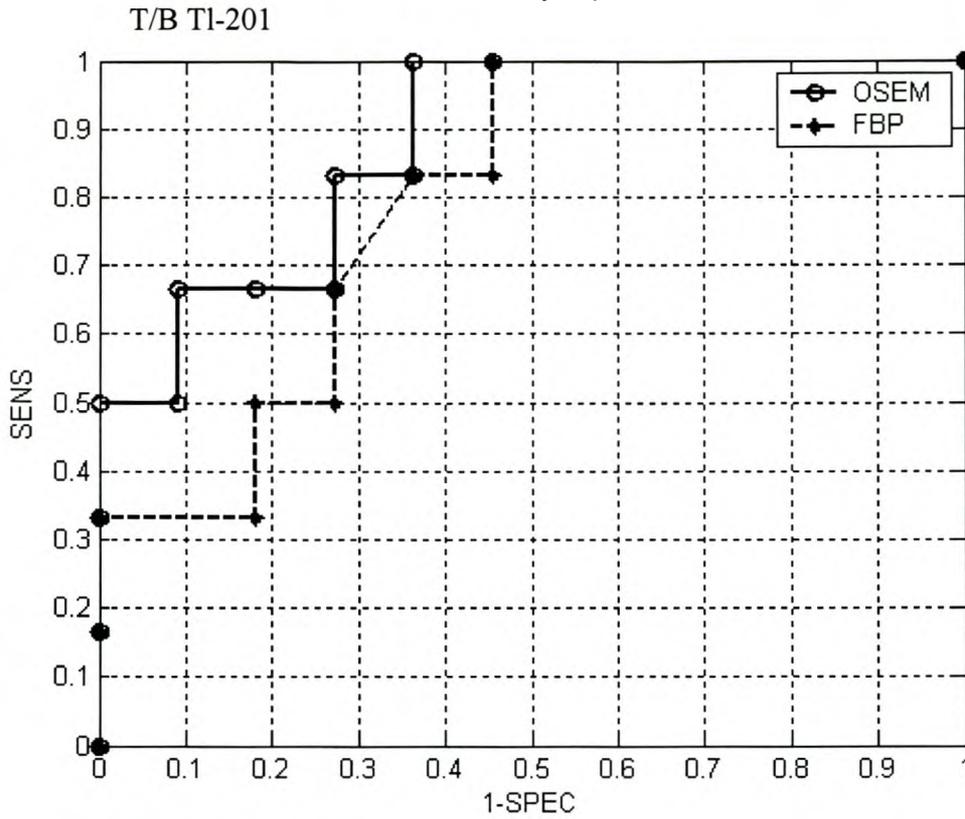


Figure 6.11 shows the ROC curves for OSEM (full line) and FBP (dashed line) in the case of Tl-201 (upper panel) and Tc-99m MIBI (lower panel) using the T/B ratio as threshold.

CHAPTER 7: DISCUSSION

7.1 OSEM versus FBP

In this study, 33 patients with single pulmonary nodules (SPN) were examined using Tl-201 and Tc-99m MIBI. SPECT images were acquired and these were reconstructed using both iterative reconstruction (ordered subsets expectation maximisation - OSEM) and filtered backprojection.

To date, most clinical studies are performed primarily using filtered backprojection (FBP). This algorithm is fast and yields reliable quantitative results. However it tends to produce streak artefacts and low signal-to-noise ratio (SNR) in poor statistic studies. FBP has well understood noise characteristics; in fact one can easily compute the noise present in FBP images^{72,73}. Iterative algorithms like ordered subsets-expectation maximisation (OSEM), however, are non-linear, and their noise properties are far more complex⁷⁴. As a result, the two reconstruction algorithms produce different noise levels in the same image when applied.

The elimination of streak artefacts with the use of iterative methods has been shown to minimise false positive results⁷⁵ as well as false negative results when lesions were situated in the vicinity of hot organs such as the bladder. In this study, FBP tended to have higher SNR than OSEM when a lesion was close to a hot background (for example the heart, liver or vertebrae). This was probably due to streak artefact formation.

Iterative reconstruction algorithms, like OSEM, take into account the positivity constraint which ensures that all pixels have a non-negative value, which is reasonable because they represent activity distribution; this however is not guaranteed by FBP⁷⁶. Nuyts et al.⁷⁷ showed that with images where attenuation has not been corrected for, the non-negativity constraint interfered with the attenuation artefact resulting in loss of information. A new maximum-likelihood (NEG-ML)⁷⁷ that allows negative reconstruction values can be used to minimise this decrease in image quality. Though FBP allows negative values, its

response to the remaining inconsistencies of the data differs from that of NEG-ML due to its different data weighting, resulting in poorer visual quality.

An evaluation of maximum likelihood-expectation maximisation (MLEM) and FBP is complicated by the fact that the quality of reconstruction can depend to a larger extent on the particulars of the implementation. With MLEM, noise character and resolution are affected by the point at which iterations are stopped. Studies done have shown that MLEM resulted in better image contrast, signal-to-noise ratio and resolution as a function of the number of iterations^{65,78}. In this study OSEM showed better SNR in 9/17 (53%) of the lesions detected by Tl-201 and in 15/21 (71%) of the lesions detected by Tc-99m MIBI irrespective of the status of the lesion.

Noise has been observed to worsen with increasing number of iterations^{79,80}. Images of better visual quality are produced if iteration is stopped at some intermediate point. Resolution on the other hand has been shown to improve with iteration.

In a phantom and clinical study, Gutman et al.⁸¹ showed that OSEM resulted in a marked increase in contrast in comparison to FBP when more than 24 iterations were used but reached a plateau after 40 iterations. Noise was found to be stable up to 40 iterations. The optimal compromise between contrast recovery and noise level was obtained for OSEM between 32 and 40 iterations for the phantom study. Possible ways to avoid increase in image noise with increase in iterations, is to limit possible reconstructions to the ones which are smooth enough⁷⁹. A second solution is to perform many iterations and post filter the reconstruction. A third way is stopping the reconstruction based on a stopping rule, before noise degrades the image quality of the reconstruction^{82,83}. For clinical use, mostly the post filtering method is used because the smoothness of the image can be chosen by using another cut-off frequency of the filter without repeating the reconstruction. In our study, after 6 x 8 iterations, post filtering was done by applying a Butterworth filter, cut-off frequency 0.6/cm and of the order of 3. This decreased noise at the expense of resolution. However, since there was no matching of the resolution between OSEM and FBP in our study, no emphasis was placed on this reduction.

Another particular feature of MLEM which can affect image quality is the specification of the probability matrix⁸⁴. This matrix is a discrete representation of the system transfer function and is intended to model the physical effects of photon detection including attenuation, scatter and detection response. Including these effects in the reconstruction results in a more accurate quantification of the lesion. In practice, this is difficult to do and an approximation is done using simple assumptions. In our study, scatter and attenuation were not corrected for and this probably affected the comparison between the two reconstruction algorithms. Though non-uniform attenuation correction can be done with the Hermes system, this needs a transmission source for accurate attenuation correction which was not available at Tygerberg Hospital. It was also noted that when data was transferred from the Apex to the Hermes system, it was necessary to retain all the processing parameters because several variables were changing simultaneously. Although ignoring attenuation leads to an artefact in the reconstructed images, these images do still provide diagnostic information. Attenuation eliminates a fraction of photons resulting in an artefact that underestimates the actual activity. In regions of non-uniform attenuation like the thorax, it is possible that foci of increased tracer uptake can disappear in images reconstructed without attenuation correction⁸⁵, decreasing the detection ability of the algorithm. In our study, detection was found to be equal between OSEM and FBP, meaning that the effect of lack of attenuation correction affected both equally. Attenuation has also been shown to have an additive effect whereby negative values are added to regions where attenuation is not negligible and that are surrounded by activity⁷⁷. This effect is somewhat similar to background subtraction (often applied in planar scintigraphy) and produces an apparent increase in tumour-to-background (T/B) ratio as observed by several studies^{66,86,87}. This apparent increase in T/B ratio is to be expected in our study as the data was not corrected for attenuation and it should affect both algorithms. However, since this affects all lesions and since it is not dependent on the type of nodule, it is not expected to change the observations. Although attenuation correction is necessary for accurate quantification, it has been shown to increase noise in the corrected images with loss of contrast. It also results in increased scanning time, more so with positron emission tomography (PET). Furthermore, some studies done based on

numeric measures ^{86,88} and human evaluation ⁸⁹ have shown a mixed or no benefit of performing attenuation correction for whole body PET. Glenn et al. found that attenuation correction, while improving OSEM images significantly, did not have the same impact on the FBP images. Attenuation correction undoubtedly would have optimised our iterative algorithm resulting in possibly even better performance in comparison to FBP.

On the other hand with FBP, image quality is greatly affected by the choice of filter and the cut-off frequency. In general, factors such as lesion size, contrast, shape, total counts and background source can affect the relative performance of these reconstruction algorithms but since these factors were the same for both reconstruction algorithms their impact is expected to be generally similar. In this study, the region of interest was first identified in the OSEM images and mirrored onto the FBP images. This could have introduced bias in the results but it cannot be ascertained.

7.2 Lesion detection

Tumour detection depends on contrast between the tumour activity and the background and on image noise. The lower the noise, the easier the detection. Tumour contrast is determined by the physiology of the tumour cells, that is, how much of the radiopharmaceuticals are taken up by the tumour. Noise is affected by the reconstruction algorithm used. Riddell et al. ⁹⁰ quantified noise in clinical images reconstructed with both OSEM and FBP and found that noise did not vary widely over each FBP image even as the image intensity varied, causing signal-to-noise ratio to be worse in low activity regions such as the lung. In contrast, OSEM showed high noise in hot regions and low noise in cold regions. As a result, OSEM was found to have a better SNR than FBP in these latter regions of the image like for example the lungs (160% improvement) and less dramatic improvement in the hotter areas (25% improvement) like for example liver. In areas of localised high intensity, FBP gave a better SNR than OSEM. In this study, FBP

was found to have a higher SNR in comparison to OSEM in 8/17 lesions detected by Tl-201. Of note is that six of these nodules were 'hot' with SNR of greater than 2.5 and four of them were both 'hot' and close to a hot background.

7.3 Tuberculosis

Tl-201 is taken up more in tuberculosis lesions (TB) in comparison to Tc-99m MIBI. The former has been shown to be taken up significantly in granulomatous lesions like tuberculosis and sarcoidosis⁹¹ and has been reported to be of value in the evaluation of disease activity⁹². A number of TB nodules were found to have significant uptake of Tl-201. This resulted in some TB nodules having high SNR and T/B ratios, comparable to those of malignant nodules. The differentiation of tuberculosis from malignant nodules remains a diagnostic problem. Studies have implicated the use of Tc-99m MIBI in the evaluation of patients with TB because the uptake is observably high and proportional to activity⁹³. Utilization of PET scanning with F-18 FDG to differentiate malignant from benign (except TB) is well established⁹⁴ but remains a problem in tuberculosis.

7.4 ROC analysis

The receiver operating characteristic (ROC) curves were used to analyse the performance of OSEM in comparison to FBP. Visually analysing the curves, OSEM was found to perform better than FBP in Tl-201 images at almost all the thresholds of SNR and T/B ratio, however at the upper threshold limits the performance equalises. The area under the curve (AUC) for OSEM was found to be greater than that for FBP, for both SNR and T/B ratios. Although the difference was found to be statistically not significant ($p=0.10$), a clear tendency can be seen. Theoretically, this means that Tl-201 in conjunction with OSEM could improve diagnosis of malignant nodules from benign ones. Since this analysis did not include TB, it is not applicable to TB nodules. Tc-99m MIBI did not show a significant difference in the accuracy of the two reconstruction algorithms. This

was confirmed by the AUC which showed a considerably insignificant difference ($p=0.62$) for SNR thresholds and equal AUC for the T/B ratio threshold. The reason for this difference between Tl-201 and Tc-99m MIBI in this study could be that the latter has been shown to accumulate significantly less in primary lung carcinoma compared to Tl-201⁵².

Cut-off values for differentiation of malignant from benign lesions vary. Higashi et al.²⁰ showed early ratios of 1.95 ± 0.69 for malignant lesions and ratios of 1.78 ± 0.28 for benign lesions using Tl-201. These ratios have been shown to vary according to the level of cell differentiation. Yamamoto et al.⁹⁵ showed T/B ratios of early images as high as 2.87 ± 0.75 in the poorly differentiated groups using Tl-201 and these ratios were significantly lower for Tc-99m MIBI.

In this study, at these comparably high T/B ratios, it can be seen that OSEM and FBP perform equally well. Of note is that, at these threshold levels, the specificity is increased at the expense of sensitivity and clinically this is suboptimal because a diagnostic procedure with considerably high sensitivity and specificity would be preferred. As T/B ratio threshold, a critical cut off of 1.5 seems more appropriate for our Tl-201 studies. The sensitivity is maintained at about 65% and specificity at 90% for OSEM, whilst for FBP the values are 50% and 70% respectively. It can be observed that for this population of patients, Tl-201 images reconstructed with OSEM might improve accuracy of differentiating malignant nodules from benign ones excluding tuberculosis. A high specificity of 90%, seen with OSEM, means that less patients with benign nodules will have invasive procedures done on them. However, more importantly, the sensitivity of Tl-201 improves with OSEM which means more patients with malignant nodules will be correctly diagnosed.

At the T/B ratio cut-off value of 1.5, the false positive fraction of tuberculosis is found to be equal (20%) for these for OSEM and FBP.

For Tc-99m MIBI, sensitivity is lower at 55%, at cut-off threshold of 1.5 and is found to be equal for both reconstruction algorithms. However, specificity is different between the algorithms: higher for FBP (80%) compared to 75% for OSEM. It can be seen clearly that the performance of the two reconstruction algorithms is not that different when using Tc-99m MIBI. Of note is that for our study, detection sensitivity is the same for both OSEM and FBP with differences being seen in the ability to differentiate malignant lesions from benign lesions.

Similar studies to compare these two reconstruction algorithms have been done. Of note is that in most of them PET is used instead of SPECT with different reconstruction parameters like number of iterations, type of filter used for post filtering and attenuation correction. OSEM has been observed to provide images of better visual quality, but with no significant difference in detection sensitivity^{81,88,78} whilst others have shown no significant difference between OSEM and FBP^{96,64}. Though direct comparison of these studies with our study is not practical, as many of the reconstruction parameters are different, similar findings can be expected as the basic reconstruction algorithms are the same.

7.5 Conclusion

This study was done to investigate the effect of iterative reconstruction (OSEM) and FBP on the diagnosis of single pulmonary nodules. This effect was analysed using ROC curves with SNR and T/B ratios as the varied thresholds. There is a tendency that the use of OSEM improves the diagnostic accuracy to distinguish between malignant and benign lung nodules, using SNR ratios, in comparison with FBP when using Tl-201 but not for Tc-99m-MIBI. However, uptake in TB lesions is high, more so with Tl-201, making differentiation from malignancy difficult irrespective of the reconstruction algorithm applied.

7.6 Suggestions for further research

The results of this study can be further improved if more patients are included. We hypothesize that the difference between OSEM and FBP for Tl-201 will become significant by increasing the statistical power.

Furthermore, it is expected that optimising the iterative algorithm by incorporating image degrading effects into the reconstruction will further improve quantification and will increase the accuracy of this technique.

Calculating the retention index has been shown to improve the diagnostic ability of Tl-201⁹⁷, and it would be interesting to see if this, combined with OSEM, could further improve diagnostic ability especially with reference to differentiation between tuberculosis and malignancy.

REFERENCES

-
- ¹ Yankelevitz DF, Henschke CI. Small solitary pulmonary nodules . Radiologic Clinics of North America 2000; 38: 471-478
 - ² Tan BB, Flaherty KR, Kazerooni EA, Iannettoni MD. The solitary nodule. Chest 2003; 123: 89S-96S
 - ³ Caskey CI, Zerhouni EA. The solitary pulmonary nodule. Seminars in Roentgenology 1990; 25: 85-95
 - ⁴ Swensen SJ, Jett JR, Payne WS, Viggiano RW, Paiolero PC, Trastek Vf. An integrated approach to evaluation of the solitary pulmonary nodule. Mayo clinic Proceedings 1990; 65: 173-186
 - ⁵ Minai OA, Raja S, Mehta AC, Sullivan EJ, Khan SU, Dasgupta A, Arroliga AC. Role of Tc-99m MIBI in the evaluation of single pulmonary nodules : a preliminary report. Thorax 2000; 55: 60-62
 - ⁶ Rivera MP, Detterbeck F, Mehta AC; American College of Chest Physicians. Diagnosis of lung cancer: the guidelines. Chest 2003; 123: 129S-136S.
 - ⁷ Munden RF, Pugatch RD, Liptay MJ, Sugarbaker DJ, Le LU. Small pulmonary lesions detected at CT: clinical importance. Radiology 1997; 202: 105-110
 - ⁸ Mountain CF. Revisions in the international system for staging lung cancer. Chest 1997; 111: 1710-1717
 - ⁹ Solitary pulmonary nodule. Observe, operate, or what? Chest 1982; 81: 662-663
 - ¹⁰ Stitik FP, Tockman MS. Radiographic screening in the early detection of lung cancer. Radiological clinics of North America 1978; 16: 347-366
 - ¹¹ Berger WG, Erly WK, Krupinski EA, Standen JR, Stern RG. The solitary pulmonary nodule on chest radiography: can we really tell if the nodule is calcified? American Journal of Radiology 2001; 176: 201-204

-
- ¹² Gurney JW. Determining the likelihood of malignancy in solitary pulmonary nodules with Bayesian analysis. Part 1: Theory. *Radiology* 1993; 186: 405-413
- ¹³ White PG, Adams H, Crane MD, and Butchart EG. Preoperative staging of carcinoma of the bronchus: can computed tomographic scanning reliably identify stage III tumours? *Thorax* 1994; 49: 951-957
- ¹⁴ Leef JL 3rd, Klein JS. The solitary pulmonary nodule. *Radiologic clinics of North America* 2002; 40: 123-143
- ¹⁵ Zerhouni EA, Stitik FP, Siegelman SS, Naidich DP, Sagel SS, Proto AV, Muhm JR, Walsh JW, Martinez CR, Heelan RT, et al. CT of the pulmonary nodule: a cooperative study. *Radiology* 1986; 160: 319-327
- ¹⁶ Woodring JH, Fried AM. Significance of wall thickness in solitary cavities of the lung: a follow up study. *American journal of Roentgenology* 1983; 140: 473-474
- ¹⁷ Abdel-Dayem HM, Scott A, Macapinlac H, Larson S. Tracer imaging in lung cancer. *European journal of Nuclear Medicine* 1994; 21: 57-81
- ¹⁸ Lowe VJ, Fletcher JW, Gobar L, Lawson M, Kirchner P, Valk P, Karis J, Hubner K, Delbeke D, Heiberg EV, Patz EF, Coleman RE. Prospective investigation of positron emission tomography in lung nodules.. *Journal of Clinical Oncology* 1998; 16: 1075-1084
- ¹⁹ Miettinen OS. Screening for lung cancer. *Radiologic Clinics of North America* 2000; 38: 479-486
- ²⁰ Higashi K, Ueda Y, Sakuma T, Seki H, Oguchi M, Taniguchi M, Taki S, Tonami H, Katsuda S, Yamamoto I. Comparison of F-18-FDG PET and Tl-201 SPECT in the evaluation of pulmonary nodules. *Journal of Nuclear Medicine* 2001; 42: 1489-1496
- ²¹ Conces DJ jr, Tarver RD, Gray WC, Percy EA. Treatment of pneumothoraces utilising small caliber chest tubes. *Chest* 1988; 94: 55-57
- ²² Kubota K. Changing pattern of lung cancer and its imaging: ²⁰¹Tl SPECT versus [¹⁸F]FDG PET. *Journal of Nuclear Medicine* 2001; 42: 1497-1498

-
- ²³ Bracewell R, Riddle A. Inversion of fan beam scans in radio astronomy. *Astrophysics Journal* 1967; 150: 427-434
- ²⁴ Shepp LA, Logan BF. The Fourier reconstruction of head section. *IEEE Transactions on Nuclear Science* 1974; NS:21-43
- ²⁵ Groch MW, Erwin WD. SPECT in 2000: basic principles. *Journal of Nuclear Medicine Technology* 2000; 28: 233-244
- ²⁶ P Zanzonico Technical requirement for SPECT: instrumentation, Data processing and Quality control in *Clinical SPECT imaging*. Kramer EL, Sanger J, eds. New York, NY: Raven Press 1995; 7-41
- ²⁷ Bailey DL, Parker JA Single photon emission tomography in *Nuclear Medicine in clinical diagnosis and treatment*. Murray IPC and Ell PJ, eds. Churchill Livingstone, Edinburgh 1994; 1315-1326
- ²⁸ Groch M W, Erwin W D. Single-photon emission computed tomography in the year 2001: instrumentation and quality control. *Journal of Nuclear Medicine Technology* 2001; 29: 12-18
- ²⁹ Nema Standards Publication No NU1-1994. *Performance measurement of scintillation cameras*. Published by National Electrical Manufactures Association, Washington DC 1994.
- ³⁰ Owunwane A, Patel M, Sadeck S. Handbook of radiopharmaceuticals. Chapman & Hall Medical, London 1995; 120-131
- ³¹ Abdel-Dayem H, Larson SM, Macapinlac H, Scott A. Thallium-201 chloride: a tumour imaging agent in *Nuclear Medicine in clinical diagnosis and treatment*. Murray IPC and Ell PJ, eds. Churchill Livingstone, Edinburgh 1994; 727-735
- ³² Strauss HW, Pitt B. Thallium-201 as a myocardial imaging agent. *Seminars of Nuclear Medicine* 1977; 7:49-58
- ³³ Caluser C, Macapinlac H, Healey J, Ghavimi F, Meyers P, Wollner N, Kalaigian J, Kostakoglu L, Abdel-Dayem HM, Yeh SD, et al. The relationship between thallium

uptake, blood flow and blood pool activity in bone and soft tissue tumors. *Clinical Nuclear Medicine* 1992; 17: 565-572

³⁴ Sessler MJ, Geck P, Maul FD, Hor G, Munz DL. New aspects of cellular thallium uptake: $Tl^{+}-Na^{+}-2Cl^{-}$ -cotransport is the central mechanism of ion uptake. *Journal of Nuclear Medicine* 1986; 25: 24-27

³⁵ Schuster DM, Alazraki N. Gallium and other agents in diseases of the lung. *Seminars in Nuclear Medicine* 2002; 32: 193-211

³⁶ Thrall JH and Ziessman HA. *The Requisites: Nuclear Medicine*. Mosby-Year Book, St.Louis 1995; 171-190

³⁷ Waxman AD. Thallium-201 in nuclear oncology. in *Nuclear Medicine Annual*. Freeman LM (ed), Raven , New York 1991; 193-209

³⁸ Mountz JM, San Pedro EC. Basis and clinical application of functional brain imaging. in *The pathologic basis of Nuclear Medicine*. Elgazzar A (ed), Springer Verlag – Berlin 2001; 294-318

³⁹ Gungor F, Bezircioglu H, Guvenc G, Tezcan M, Yildiz A, Uluc E, Isisag A. Correlation of thallium-201 uptake with proliferating cell nuclear antigen in brain tumours. *Nuclear Medicine Communications* 2000; 21: 803-810

⁴⁰ ICRP 53 Radiation Dose to Patients from Radiopharmaceuticals. Pergamon Press (Oxford 1988)

⁴¹ Sehweil A, McKillop JH, Ziada G, Al-Sayed M, Abdel-Dayem H, Omar YT. The optimum time for tumour imaging with Thallium-201. *European Journal of Nuclear Medicine* 1988; 13: 527-529

⁴² Chen DCP, Ma GQ, Ansari A, Hung GL, Stewart CA, Kawada T, Siegel A. Optimal imaging time for thallium-201 as a tumour agent in patients with lymphoma. *Journal of Nuclear Medicine* 1992; 33:844 (abstract)

⁴³ Ganz WI, Nguyen TQ, Benedetto MP, Mnaymnen W, Friden A, Topchik S, Serafini A, Sfakianakis G. Use of early, late and SPECT thallium imaging in evaluating activity of soft tissue and bone tumours. *Journal of Nuclear Medicine* 1993; 43:33P (abstract)

-
- ⁴⁴ Coakley AJ, Kettle AG, Wells CP, O'Doherty MJ, Collins RE. Tc-99m sestamibi, a new agent for parathyroid imaging. *Nuclear Medicine Communications* 1989; 10: 791-794
- ⁴⁵ Macapinlac H, Finlay J, Yeh SDJ, Scott A, DelaPaz R, Lindsey K, Finn RA, Muraki A, Larson S, Abdel-Dayem H et al. Comparison of thallium-201 SPECT and F-18 FDG PET with MRI (Gd-DTPA) in the evaluation of recurrent supratentorial and infratentorial brain tumours. *Journal of Nuclear Medicine* 1992; 33:867 (abstract)
- ⁴⁶ Elgazzar AH, Malki AA, Abdel-Dayem HM, Mahmoud A, Sahweil A, Razzak S, Jahan S, el-Sayed M, Omar YT. Role of thallium-201 in the diagnosis of solitary bone lesions. *Nuclear Medicine Communications* 1989; 10: 477-485
- ⁴⁷ Van der Wall HD, Murray IP, Huckstep RL, Philips RL. The role of thallium scintigraphy in excluding malignancy in bone. *Nuclear Medicine Communications* 1993; 18: 551-557
- ⁴⁸ Cox PH, Belfer AJ, van der Pompe WB. Thallium-201 chloride uptake in tumours, a possible complication in heart scintigraphy. *British Journal of Radiology* 1976; 49: 767-768
- ⁴⁹ Tonami N, Shuke N, Yokoyama K, Seki H, Takayama T, Kinuya S, Nakajima K, Aburano T, Hisada K, Watanabe Y. Thallium-201 single photon emission computed tomography in the evaluation of suspected lung cancer. *Journal of Nuclear Medicine* 1989; 30: 997-1004
- ⁵⁰ Tonami N, Yokoyama K, Shuke N, Taki J, Kinuya S, Miyauchi T, Michigishi T, Aburano T, Hisada K, Watanabe Y, et al. Evaluation of suspected malignant pulmonary lesions with Tl-201 single photon emission computed tomography. *Nuclear Medicine Communications* 1993; 14: 602-610
- ⁵¹ Hassan IM, Sahweil A, Constantinides C, Mahmoud A, Nair M, Omar YT, Abdel-Dayem HM. Uptake and kinetics of Tc-99m hexakis 2-methoxy isobutyl isonitrile in benign and malignant lesions in the lungs. *Clinical Nuclear Medicine* 1989; 14: 333-340

-
- ⁵² Nishiyama Y, Kawasaki Y, Yamamoto Y, Fukunaga K, Satoh K, Takashima H, Ohkawa M, Tanabe M. Technetium-99m-MIBI and thallium-201 scintigraphy of primary lung cancer. *Journal of Nuclear Medicine* 1997; 38: 1358-1361
- ⁵³ Piwnica-Worms D, Holman BL. Noncardiac applications of hexakis (alkylisonitrile) technetium-99m complexes. *Journal of Nuclear Medicine* 1990; 31: 1166-1167
- ⁵⁴ Chiu ML, Kronauge JF, Piwnica-Worms D. Effect of mitochondrial and plasma membrane potentials on accumulation of hexakis (2-methoxyisobutylisonitrile) technetium(I) in cultured mouse fibroblasts. *Journal of Nuclear Medicine* 1990; 31: 1646-1653
- ⁵⁵ Ballinger JR, Hua HA, Berry BW, Firby P, Boxen I. ⁹⁹Tcm-sestamibi as an agent for imaging P-glycoprotein-mediated multi-drug resistance: in vitro and in vivo studies in a rat breast tumour cell line and its doxorubicin-resistant variant. *Nuclear Medicine Communications* 1995; 16: 253-257
- ⁵⁶ Wang H, Maurea S, Mainolfi C, Fiore F, Gravina A, Panico MR, Bazzicalupo L, Salvatore M. Tc-99m MIBI scintigraphy in patients with lung cancer. Comparison with CT and fluorine-18 FDG PET imaging. *Clinical Nuclear Medicine* 1997; 22: 243-249
- ⁵⁷ Bruyant PP. Analytic and iterative reconstruction algorithms in SPECT. *Journal of Nuclear Medicine* 2002; 43: 1343-1358
- ⁵⁸ Goris ML, Briandet PA. *A clinical and mathematical introduction to computer processing of scintigraphic images*. Raven Press New York 1983; 73-79
- ⁵⁹ Germano G. The technical aspects of myocardial SPECT imaging. *Journal of Nuclear Medicine* 2001; 42; 1499-1507
- ⁶⁰ Blocklet D, Seret A, Popa N, Schoutens A. Maximum-likelihood reconstruction with ordered subsets in bone SPECT. *Journal of Nuclear Medicine* 1999; 40: 1978-1984.
- ⁶¹ Moore SC, Brunelle JA, Kirsch CM. Quantitative multi-detector emission computerized tomography using iterative attenuation compensation. *Journal of Nuclear Medicine* 1982; 23: 706-714

-
- ⁶² English RJ, Brown SE. *SPECT: single photon emission computed tomography: a primer*. New York, NY: Society of Nuclear Medicine 1986; 9-24
- ⁶³ Hutton BF, Hudson HM, Beekman FJ. A clinical perspective of accelerated statistical reconstruction. *European Journal of Nuclear Medicine* 1997; 24: 797-808
- ⁶⁴ Wells RG, King MA, Simkin PH, Judy PF, Brill AB, Gifford HC, Licho R, Pretorius PH, Schneider PB, Seldin DW. Comparing filtered backprojection and ordered-subsets expectation maximization for small-lesion detection and localization in ⁶⁷Ga SPECT. *Journal of Nuclear Medicine* 2000; 41: 1391-1399
- ⁶⁵ Miller TR, Wallis JW. Clinically important characteristics of maximum-likelihood reconstruction. *Journal of Nuclear Medicine* 1992; 33: 1678-1684
- ⁶⁶ Lonneux M, Borbath I, Bol A, Coppens A, Sibomana M, Bausart R, Defrise M, Pauwels S, Michel C. Attenuation correction in whole-body FDG oncological studies: the role of statistical reconstruction. *European Journal of Nuclear Medicine* 1999; 26: 591-598
- ⁶⁷ Todd-Pokropek A. Theory of tomographic reconstruction. in *Tomographic Methods in Nuclear Medicine: Physical Principles, Instruments, and Clinical Applications*. Ahluwalia BD, ed. CRC Press Boca Raton, FL 1989; 3-33.
- ⁶⁸ Meikle SR, Hutton BF, Bailey DL, Hooper PK, Fulham MJ. Accelerated EM reconstruction in total-body PET: potential for improving tumour detectability. *Physics in Medicine and Biology* 1994; 39: 1689-1704
- ⁶⁹ Hansen CL. Digital image processing for clinicians, part II: Filtering. *Journal of Nuclear Cardiology* 2002; 9: 429-437
- ⁷⁰ Hanley JA and McNeil BJ. A method of comparing the areas under the receiver operating characteristics curves derived from the same cases. *Radiology* 1983; 148: 839-843
- ⁷¹ Hanley JA and McNeil BJ. The meaning and use of the area under a receiver operating characteristic (ROC) curve. *Radiology* 1982; 143: 29-36.

-
- ⁷² Alpert NM, Chesler DA, Correia JA, Ackerman RH, Chang JY, Finklestein S, Davis SM, Brownell GL and Taveras JM. Estimation of local statistical noise in emission computed tomography. *IEEE Transactions on Medical Imaging* 1982; MI-1:142-146
- ⁷³ Pajevic S, Daube –Witherspoon ME, Bacharach SL, Carson RE. Noise characteristics of 3-D and 2-D PET images. *IEEE Transactions on Medical Imaging* 1998; 17: 9-23
- ⁷⁴ Barrett HH, Wilson DW, Tsui BMW. Noise properties of the EM algorithm. I. Theory. *Physics in Medicine and Biology* 1994; 39: 833-846
- ⁷⁵ Strauss LG. Fluorine-18 deoxyglucose and false-positive results: a major problem in the diagnostics of oncological patients. *European Journal of Nuclear Medicine* 1996; 23: 1409-1415
- ⁷⁶ Vandenberghe S, D'Asseler Y, Van de Walle R, Kauppinen T, Koole M, Bouwens L, Van Laere K, Lemahieu I, Dierckx RA. Iterative reconstruction algorithms in nuclear medicine. *Computerized Medical Imaging & Graphics* 2001; 25:105-111
- ⁷⁷ Nuyts J, Stroobants S, Dupont P, Vleugels S, Flamen P, Mortelmans L. Reducing loss of image quality because of the attenuation artifact in uncorrected PET whole-body images. *Journal of Nuclear Medicine* 2002; 43: 1054-1062
- ⁷⁸ Paul AK, Tatsumi M, Yutani K, Fujino K, Hashikawa K, Nishimura T. Effects of iterative reconstruction on image contrast and lesion detection in gamma camera coincidence imaging in lung and breast cancers. *Nuclear Medicine Communications* 2002; 23: 103-110.
- ⁷⁹ Snyder DL, Miller MI. The use of sieves to stabilize images produced with the EM algorithm for emission tomography. *IEEE Transactions on Nuclear Science* 1985; NS-32: 3864-3872
- ⁸⁰ Veklerov E, Llacer J. Stopping rule for the MLE algorithm based on statistical hypothesis testing. *IEEE Transactions on Medical Imaging* 1987; MI-6: 313-319
- ⁸¹ Gutman F, Gardin I, Delahaye N, Rakotonirina H, Hitzel A, Manrique A, Le Guludec D, Vera P. Optimisation of the OS-EM algorithm and comparison with FBP for image

reconstruction on a dual-head camera: a phantom and a clinical 18F-FDG study. *European Journal of Nuclear Medicine and Molecular Imaging* 2003; 30:1510-1519

⁸² Veklerov E, Llacer J, Hoffman EJ. MLE reconstruction of a brain phantom using a Monte Carlo transition matrix and a statistical stopping rule. *IEEE Transactions on Nuclear Science* 1988; NS-35: 603-607

⁸³ Llacer J, Veklerov E. Feasible images and practical stopping rules for iterative algorithms in emission tomography. *IEEE Transactions on Medical Imaging* 1989; 8: 186-193

⁸⁴ Shepp LA, Vardi Y. Maximum likelihood reconstruction for emission tomography. *IEEE Transactions on Medical Imaging* 1982; MI-1: 113-122

⁸⁵ Bai C, Kinahan PE, Brasse D, Comtat C, Townsend DW, Meltzer CC, Villemagne V, Charron M, Defrise M. An analytic study of the effects of attenuation on tumor detection in whole-body PET oncology imaging. *Journal of Nuclear Medicine* 2003; 44: 1855-1861

⁸⁶ Imran MB, Kubota K, Yamada S, Fukuda H, Yamada K, Fujiwara T, Itoh M. Lesion-to-background ratio in nonattenuation-corrected whole-body FDG PET images. *Journal of Nuclear Medicine* 1998; 39: 1219-1223

⁸⁷ Bengel FM, Ziegler SI, Avril N, Weber W, Laubenbacher C, Schwaiger M. Whole-body positron emission tomography in clinical oncology: comparison between attenuation-corrected and uncorrected images. *European Journal of Nuclear Medicine* 1997; 24: 1091-1098

⁸⁸ Riddell C, Jousse F, Aloj L, et al. Attenuation correction vs. no attenuation correction : a signal to noise analysis in FDG PET wholebody images. *Journal of Nuclear Medicine* 1998; 39(suppl): 98P.

⁸⁹ Pieterman RM, Pruijm J, Que TH, Willemsen AT, Groen HJ, Vaalburg W. Attenuation versus nonattenuation corrected whole body (WB) FDG PET in the staging of non small cell lung cancer (NSCLC). *Journal of Nuclear Medicine* 1999; 40(suppl): 139P.

⁹⁰ Riddell C, Carson RE, Carrasquillo JA, Libutti SK, Danforth DN, Whatley M, Bacharach SL. Noise reduction in oncology FDG PET images by iterative reconstruction: A quantitative assessment. *Journal of Nuclear Medicine* 2001; 42: 1316-1323.

-
- ⁹¹ Ando A, Ando I, Katayama M, Sanada S, Hiraki T, Mori H, Tonami N, Hisada K. Biodistributions of ²⁰¹Tl in tumor bearing animals and inflammatory lesion induced animals. *European Journal of Nuclear Medicine* 1987;12: 567-572
- ⁹² Utsunomiya K, Narabayashi I, Nishigaki H, Tsujimoto K, Kariyone S, Ohnishi S. Clinical significance of thallium-201 and gallium-67 scintigraphy in pulmonary tuberculosis. *European Journal of Nuclear Medicine* 1997; 24: 252-257
- ⁹³ Onsel C, Sonmezoglu K, Camsari G, Atay S, Cetin S, Erdil YT, Uslu I, Uzun A, Kanmaz B, Sayman HB. Technetium-99m MIBI scintigraphy in pulmonary tuberculosis. *Journal of Nuclear Medicine* 1996; 37:233-238
- ⁹⁴ Bakheet SM, Powe J, Ezzat A, Rostom A. F-18-FDG uptake in tuberculosis. *Clinical Nuclear Medicine* 1998; 23:739-742
- ⁹⁵ Yamamoto Y, Nishiyama Y, Fukunaga K, Kobayashi T, Satoh K, Fujita J, Ohkawa M. Evaluation of histopathological differentiation in lung adenocarcinoma patients using ²⁰¹Tl-chloride and ⁹⁹Tcm-MIBI SPET. *Nuclear Medicine Communications* 2001; 22: 539-45
- ⁹⁶ Boellard R, van Lingen A, Lammertsma AA. Experimental and clinical evaluation of iterative reconstruction (OSEM) in dynamic PET: quantitative characteristics and effects on kinetic modeling. *Journal of Nuclear Medicine* 2001; 42: 808-817
- ⁹⁷ Takekawa H, Itoh K, Abe S. Thallium-201 uptake, histopathological differentiation and Na-K ATPase in lung adenocarcinoma. *Journal of Nuclear Medicine* 1996; 37: 955-958